Article

An in vitro model of early anteroposterior organization during human development

https://doi.org/10.1038/s41586-020-2383-9

Received: 14 December 2018

Accepted: 24 April 2020

Published online: 11 June 2020

Check for updates

Naomi Moris[1,6]✉, Kerim Anlas[1,3,6], Susanne C. van den Brink[2,6], Anna Alemany[2,6], Julia Schröder[1,4], Sabitri Ghimire[1], Tina Balayo[1,5], Alexander van Oudenaarden[2,7]✉ & Alfonso Martinez Arias[1,7]✉

The body plan of the mammalian embryo is shaped through the process of gastrulation, an early developmental event that transforms an isotropic group of cells into an ensemble of tissues that is ordered with reference to three orthogonal axes[1]. Although model organisms have provided much insight into this process, we know very little about gastrulation in humans, owing to the difficulty of obtaining embryos at such early stages of development and the ethical and technical restrictions that limit the feasibility of observing gastrulation ex vivo[2]. Here we show that human embryonic stem cells can be used to generate gastruloids—three-dimensional multicellular aggregates that differentiate to form derivatives of the three germ layers organized spatiotemporally, without additional extra-embryonic tissues. Human gastruloids undergo elongation along an anteroposterior axis, and we use spatial transcriptomics to show that they exhibit patterned gene expression. This includes a signature of somitogenesis that suggests that 72-h human gastruloids show some features of Carnegie-stage-9 embryos[3]. Our study represents an experimentally tractable model system to reveal and examine human-specific regulatory processes that occur during axial organization in early development.

The body plan of mammalian embryos emerges through interactions of sequential cell-fate decisions and morphogenetic events, which have hitherto been difficult to observe in humans. Human embryonic stem (ES) cells[4] have opened up opportunities for studying early fate decisions, and have hinted at the existence of regulatory mechanisms that are specific to humans[5,6]. But in contrast to the embryo, in which proportionate populations interact with one another to generate tissues and organs, differentiation in adherent culture is heterogeneous and favours a limited number of cell types[7]. Seeding human ES cells on micropatterned surfaces yields coordinated patterns of gene expression, but without the axial organization that is characteristic of embryos[8]. However, when mouse ES cells are aggregated in suspension under defined conditions, they generate 'gastruloids', which are three-dimensional, in vitro models of mammalian development that exhibit an embryo-like spatiotemporal organization of gene expression[9,10]. We hypothesized that similar human gastruloids could be derived from human ES cells.

Generation of human gastruloids

When human ES cells in two-dimensional culture were treated with Chiron, a WNT agonist, for one day before seeding defined numbers in low-adherence plates in the presence of Chiron, they formed compact, spherical aggregates within a few hours (Fig. 1a, Extended Data Fig. 1a–c). These aggregates progressively broke symmetry and formed elongated structures, with maximal elongation at 72–96 h (Fig. 1a–d). On average, around 66% of aggregates from each experiment showed an elongated morphology at 72 h (Fig. 1e, f, Extended Data Fig. 1d; see Methods for details of classification). Although some of the structures remained elongated until 96 h, most tended to curl or retract after 72 h. Different cell lines required stimulation with different concentrations of Chiron (Extended Data Fig. 1e).

Before aggregation, pre-treated human ES cells were found to express pluripotency markers but with increased expression of mesendodermal marker genes that include *BRA* (also known as *TBXT*), *MIXL1*, *EOMES* (Extended Data Fig. 2a, Supplementary Table 1) and membrane-localized N-cadherin (CDH2) (Extended Data Fig. 2b–d). These results suggest that after pre-treatment with Chiron, human ES cells become partially primed towards a primitive-streak-like state, in agreement with observations that WNT signalling induces mesodermal differentiation of human ES cells[7,11].

Axial organization of gene expression

Polarized expression of BRA protein was detectable as early as 24 h (Extended Data Fig. 3a) overlapping a SOX2-expressing domain; by 96 h, this had resolved into distinct BRA$^+$ and SOX2$^+$ regions (Fig. 1g). All cells expressed CDH2, with higher levels in the posterior BRA- and

[1]Department of Genetics, University of Cambridge, Cambridge, UK. [2]Oncode Institute, Hubrecht Institute-KNAW (Royal Netherlands Academy of Arts and Sciences) and University Medical Center Utrecht, Utrecht, The Netherlands. [3]Present address: European Molecular Biology Laboratory (EMBL) Barcelona, Barcelona, Spain. [4]Present address: Heidelberg University, Heidelberg, Germany. [5]Present address: Universidad de las Palmas de Gran Canaria (ULPGC), Las Palmas, Spain. [6]These authors contributed equally: Naomi Moris, Kerim Anlas, Susanne C. van den Brink, Anna Alemany. [7]These authors jointly supervised this work: Alexander van Oudenaarden, Alfonso Martinez Arias. ✉e-mail: nem33@cam.ac.uk; a.vanoudenaarden@hubrecht.eu; ama11@hermes.cam.ac.uk

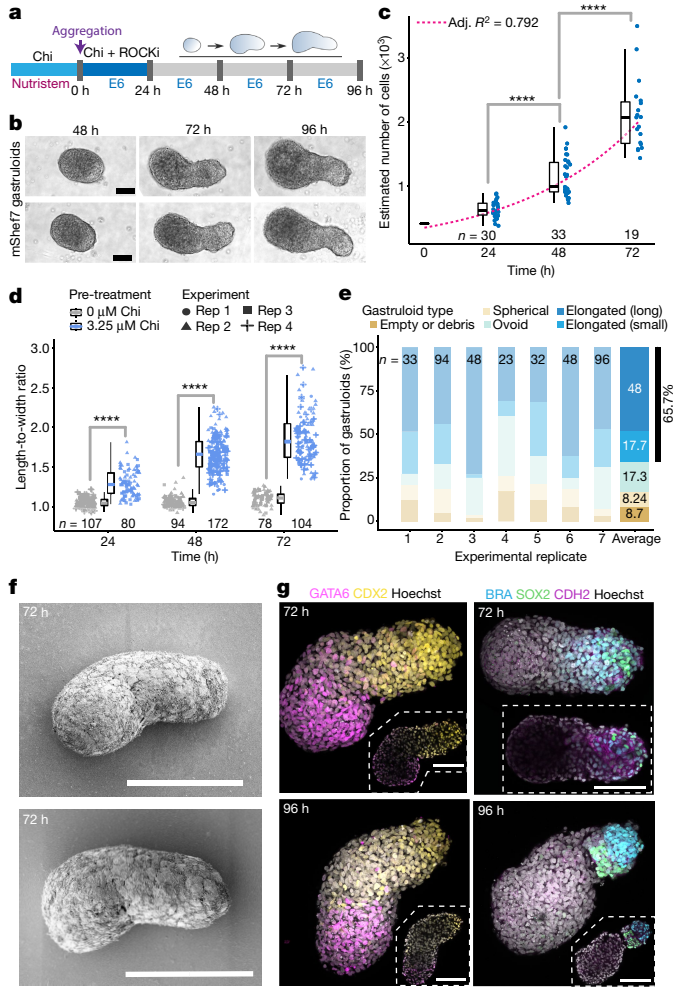

Fig. 1 | Structure and morphology of human gastruloids. a, Schematic of the human gastruloid protocol. Chi, Chiron (CHIR99021); E6, Essential 6 medium; ROCKi, ROCK inhibitor. **b**, Temporal morphology. Two representative examples from the MasterShef7 (mShef7) cell line are shown ($n = 3$ experiments). Scale bars, 200 μm. **c**, **d**, Estimated number of cells in RUES2-GLR human gastruloids (**c**) and elongation of RUES2-GLR gastruloids that were pre-treated with the indicated concentrations of Chiron (**d**). Data are from two to four independent biological replicates (rep); $^{****}P < 0.0001$ (Welch two-sided, two-sample *t*-test). Centre line, median; box, interquartile range; whiskers, range not including outliers (1.5× interquartile range). See Methods, Source Data. **e**, Proportion of elongated RUES2-GLR gastruloids at 72 h, as quantified using an automated measure of morphological elongation (see Methods for details). Left, $n = 7$ independent biological replicates; right, average proportions (percentages indicated). Representative images of each morphological elongation category are shown in Extended Data Fig. 1d. **f**, Scanning electron micrographs of RUES2-GLR gastruloids at 72 h. Two representative examples are shown ($n = 28$ gastruloids). Scale bars, 200 μm. **g**, Projections of immunofluorescence-labelled RUES2-GLR gastruloids at 72 h (top) and 96 h (bottom). Insets, individual sections (dashed lines). Scale bars, 100 μm. The number of gastruloids (n) is shown in **c**–**e**.

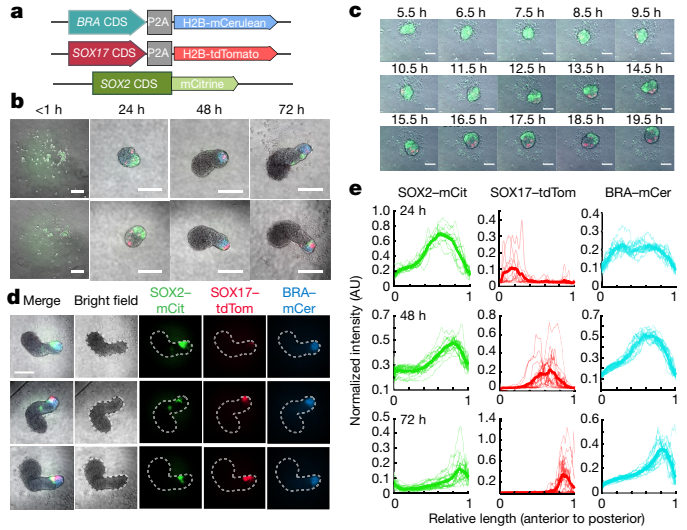

Fig. 2 | Dynamic polarization of cell types associated with three germ layers in human gastruloids. a, Schematic of the RUES2-GLR cell line. CDS, coding sequence. **b**, The temporal dynamics of RUES2-GLR human gastruloid development. Colours indicate reporter fluorescence as in **a**. Two examples are shown that are representative of at least five independent experiments. Scale bars, 200 μm. **c**, Stills from live-cell imaging of RUES2-GLR gastruloids. Colours are as in **b**. One representative example is shown from three independent experiments. Scale bars, 100 μm. **d**, Localization of the three germ-layer fluorescent reporters at 72 h. mCit, mCitrine; tdTom, tdTomato; mCer, mCerulean. Three examples are shown that are representative of at least five independent experiments. Scale bar, 100 μm. **e**, Quantification of the dynamics of reporter expression along the anteroposterior axis of elongating gastruloids. Thin lines, individual gastruloids; thicker lines, average of each time point. AU, arbitrary units.

SOX2-expressing domain (Fig. 1g, Extended Data Fig. 3b). A group of GATA6-expressing cells was localized at one end, opposite to the cells that expressed CDX2 (Fig. 1g), and this pattern was refined as the aggregates underwent elongation (Extended Data Fig. 3c–f; see Methods for details of classification). The polarization of *GATA6* was confirmed using live-cell imaging of an S4-GATA6 reporter line[12] and occurred as early as 24 h (Extended Data Fig. 3g, Supplementary Video 1). The CDX2-expressing region also contained cells that expressed BRA (Fig. 1g), suggesting that this region corresponds to a posterior embryonic identity, as co-expression of these genes is restricted to the tailbud of mammalian embryos.

To ascertain whether human gastruloids were capable of generating derivatives of the three germ layers, we used a reporter line (RUES2-GLR[13]) to identify cells expressing markers of the mesoderm (*BRA*), endoderm (*SOX17*) and neuroectoderm (*SOX2*) (Fig. 2a). Time-lapse videos of RUES2-GLR cells during aggregation (Supplementary Video 2) and elongation (Supplementary Video 3) allowed us to follow the process of symmetry-breaking and segregation of germ-layer progenitors in human gastruloids. Initially, all cells express SOX2 (Fig. 2b) before individual *SOX17*$^+$ cells emerge throughout the aggregate and SOX2 expression becomes confined to one end (Fig. 2c). Between 24 h and 48 h, *BRA* expression, which is initially low and ubiquitous, increases and becomes localized to the SOX2-expressing region of the aggregate. By 72 h, aggregates expressed *BRA* at the distal end, with neighbouring *SOX17*$^+$ and SOX2$^+$ domains (Fig. 2d). The profiles of these fluorescent reporter genes were comparable among individual gastruloids when aligned along the anteroposterior axis (Fig. 2e).

The pre-treatment with Chiron was absolutely necessary for elongation and patterned gene expression (Fig. 1d, Extended Data Fig. 1b, c). However, in our experiments, pre-treatment with WNT3A was unable to substitute for Chiron—as evidenced by a lack of elongation and absence of *BRA* expression (Extended Data Fig. 4a)—suggesting that Chiron and WNT3A have different effects in human ES cells[14]. We also found that BMP4, which is used to trigger patterned gene expression in micropatterns[8], was unable to substitute for Chiron and led to the formation of small, spherical aggregates with no discernible patterning (Extended Data Fig. 4b). These observations highlight differences in the cellular response to signals—perhaps associated with the dimensionality of the system. They also suggest that the formation of human

gastruloids is highly dependent on the signalling exposure of the initial cell population.

To further investigate how the formation of human gastruloids depends on signalling, we applied small-molecule inhibitors of BMP, WNT and Nodal signalling during pre-treatment. When RUES2-GLR cells were treated with previously used levels of Chiron in the presence of a BMP inhibitor (LDN193189) or a WNT inhibitor (XAV-939), the cells were unable to form patterned aggregates or to elongate (Extended Data Fig. 4c). Likewise, inhibition of Nodal signalling with SB431542 (hereafter, SB43) led to the formation of ovoid aggregates that co-express both SOX2 and *BRA* (Extended Data Fig. 4d)—although increasing the concentration of Chiron during aggregation increased the levels of *BRA* expression and led to robust elongation, with co-expression of *BRA* and SOX2 at the posterior pole (Extended Data Fig. 4d). These results suggest that a balance between the levels of Nodal and WNT signalling has a role in establishing cell-fate decisions and promoting elongation in human gastruloids.

Having observed this dependence on cellular signals during the formation of human gastruloids, we examined the effect of sustained gastruloid culture with retinoic acid, which is known to disrupt axial patterning and cause congenital malformations[15]. Gastruloids that were treated with retinoic acid were typically rounded, with high SOX2 expression and a strong reduction in *BRA* expression, although they had separate $CDX2^+$ and $GATA6^+$ domains (Extended Data Fig. 4e, f). This suggests that certain elements of axial patterning and organization in the human gastruloids—particularly elongation—were adversely affected by treatment with retinoic acid.

These results support the notion that the signalling environment, before and during gastruloid development, is a critical factor in establishing both the morphology and the patterning of human gastruloids.

Human gastruloid transcriptional body plan

To examine the transcriptional complexity of human gastruloids, we applied tomo-sequencing (tomo-seq)[16] to 72-h RUES2-GLR gastruloids that were pre-treated with Chiron (Methods). Two gastruloids were embedded in cryofreezing medium and sectioned (using 20-μm sections) along their anteroposterior axis, before processing each of the sections by RNA sequencing (Fig. 3a, b, Extended Data Fig. 5a, Methods).

We identified 1,023 genes with reproducible expression between the two replicates (Methods). These genes were organized into 22 main classes of expression pattern, with representatives of all three germ layers (Fig. 3c–e, Extended Data Fig. 5b, c, Supplementary Data 1, 2). Most notably, six clusters, localized to the posterior-most region of the gastruloid (clusters 0–5), contained genes with homologues that are localized to the tailbud of mouse embryos, including *BRA*, *CDX2* and *CYP26A1*. At the opposite end, we observed nine clusters (clusters 6–14) that contained genes associated with cardiac and anterior endoderm development in the mouse embryo, including *KDR*, *MEIS1*, *MEIS2*, *PBX1*, *TWIST1*, *ISL1*, *IRX1*, *IRX2*, *IRX3* and *PRDM1* (Fig. 3c, d, Supplementary Data 3). Cluster 21 was strongly enriched for genes that are involved in somitogenesis and the Notch signalling pathway.

We did not find evidence for the expression of genes associated with the development of anterior neural structures (Extended Data Fig. 6a), but observed the expression of many paralogues from the four clusters of HOX genes (Extended Data Fig. 6b). In mouse embryos, Hox genes are known to be sequentially expressed along the anteroposterior axis. In human gastruloids, HOX genes exhibit variable expression domains along the length of the anteroposterior axis, but show a somewhat broader domain of paralogues 1–5, and a more posterior-biased distribution of groups 6–8. Paralogues 9–13 were expressed at variable or low levels, or not detected (Fig. 3f, Extended Data Fig. 6b). Some posterior genes were also expressed in the anterior part of the gastruloid (for example, *HOXA9*, *HOXA10*, *HOXC9* and *HOXC10*; Fig. 3f). In the absence of an embryonic reference, it is not possible to discern whether this localization indicates an early phase in the regulation of HOX gene expression, a species difference or a feature of this model system.

The global patterns of gene expression raised the question of whether this organization reflects elements of a body plan—the blueprint for the organism. This possibility is supported by the organization of a posterior domain of gene expression in the human gastruloids (Fig. 4a, b), in which we observed a node-like transcriptional domain[17] (Fig. 4c, d, Extended Data Fig. 6c). At the anterior end, we observed the polarization of genes that are associated with the development of cardiac mesoderm[18,19] (Fig. 4e, f).

Signalling and pattern organization

One of the mechanisms by which gastruloids might establish or maintain patterning along their anteroposterior axis includes the organization of signalling components along their length. Assessing this in the tomo-seq data, we observed that several genes that encode WNT ligands were preferentially expressed at the posterior end (*WNT5A*, *WNT3A*, *WNT5B*, *LEF1* and *WNT3*) and some genes encoding BMP ligands were expressed anteriorly (*BMP2*, *BMP4* and *BMP5*; Extended Data Fig. 6d). Using a SMAD1 reporter line[20], we observed increased nuclear localization of RFP-tagged SMAD1 at the anterior end (Extended Data Fig. 6e, f). The anterior localization of BMP signalling is consistent with its function in cardiac development of the mammalian embryo. At the posterior end, we observed expression of WNT3A and LEF1, indicating WNT signalling within the posterior region (Extended Data Fig. 6g, h). In addition, we observed a peak of Nodal signalling components and targets, including *NODAL*, *LEFTY1*, *LEFTY2* and *CER1*, within the posterior region of human gastruloids (Extended Data Fig. 6i). This is consistent with a known role of WNT and Nodal signalling in the mammalian tailbud, and together the data suggest that human gastruloids might use signalling gradients along their anteroposterior axis to establish patterning.

In mouse embryos, Nodal signalling has an early role in establishing different fates along the anteroposterior axis, before becoming localized to the posterior pole and the node[21,22]. Having observed that suppression of Nodal signalling during pre-treatment could still lead to robust elongation of human gastruloids (Extended Data Figs. 4d, 7a, b), we wanted to examine the organization of gene expression in these gastruloids closely. Gastruloids that were pre-treated with both Chiron and SB43 (that is, in which Nodal signalling was inhibited) had a larger well-defined SOX2 domain at their posterior end; diffuse expression of *BRA* that approximated an anteroposterior gradient; and no detectable expression of *SOX17* compared to those pre-treated with Chiron alone (Extended Data Fig. 7b–d, Supplementary Table 2). A comparative analysis between 120-h gastruloids that were pre-treated with Chiron and SB43 and those in which Nodal signalling was not inhibited (Extended Data Figs. 7d–g, 8a–c, Supplementary Data 4, 5, Methods) showed that although 301 genes were reproducibly localized in both conditions, treatment with SB43 led to the acquisition of 944 genes with novel spatial localization and the loss of reproducible localization of 509 genes (Extended Data Fig. 7e, Supplementary Data 5). In addition, 564 genes (33%) were differentially expressed between the two treatments (Extended Data Fig. 7f, Supplementary Data 6). One cluster of genes that was lost after pre-treatment with SB43 (cluster 4; Extended Data Fig. 7g) included genes that are known to be involved in Nodal signalling, many of which are associated with the node in mammalian embryos (Supplementary Data 5)—consistent with a loss of Nodal activity. We also noticed a decrease in expression of genes associated with definitive endoderm (*SHH*, *LHX1*, *CER1*, *FOXA3*, *SORCS2* and *FOXA2*)—in line with the role of Nodal in the specification of this germ layer in mouse embryos[21]—and a loss of expression of genes associated with cardiac development (*TBX5*, *GATA6*, *LBX1* and *NKX2-5*), which is probably a consequence of the loss of induction from the endoderm[23] (Extended Data Fig. 8d, e, Supplementary Data 7).

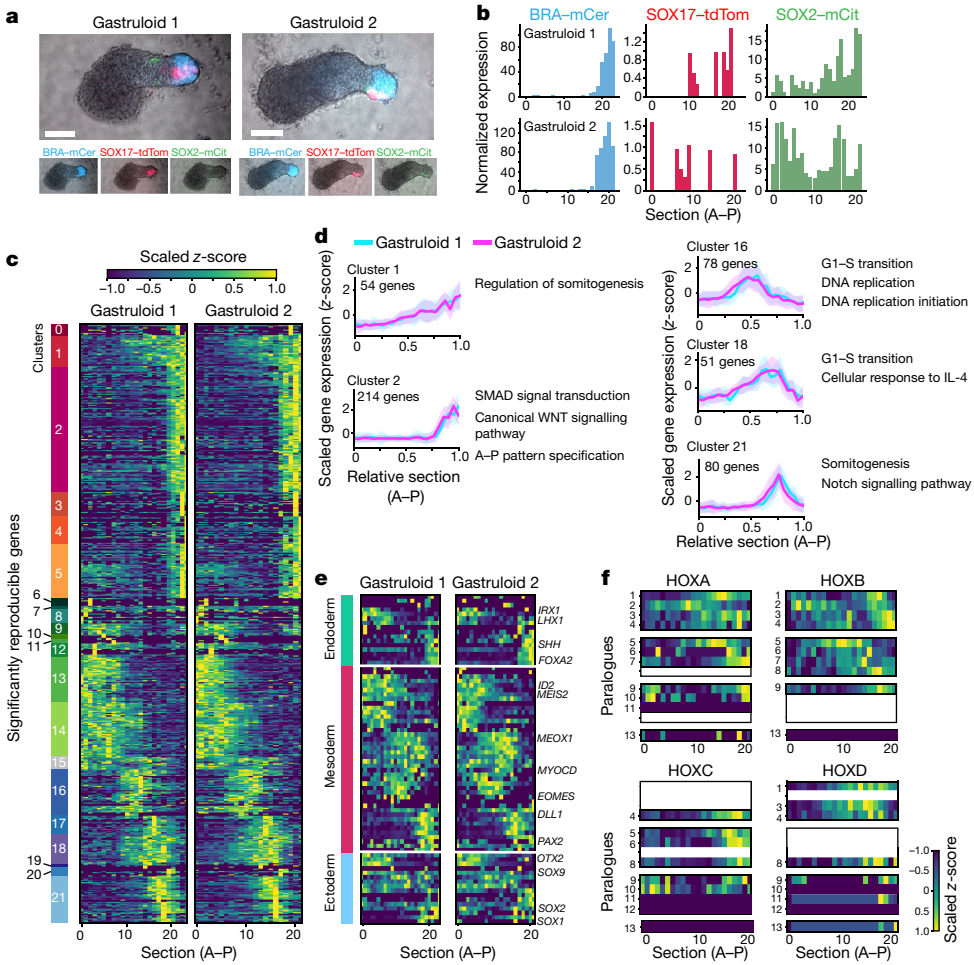

Fig. 3 | Transcriptomic anteroposterior organization of human gastruloids. a, Wide-field imaging of 72-h RUES2-GLR human gastruloids that were used for tomo-seq. Scale bars, 100 µm. **b**, mRNA expression of the fluorescent reporter transgenes along the anteroposterior (A–P) axis. **c**, Transcriptomic analysis of 1,023 significantly reproducible genes along the anteroposterior axis of two 72-h RUES2-GLR gastruloids that were pre-treated with Chiron. Coloured blocks (left) show clusters of genes with similar expression patterns (see Methods, Supplementary Data 1). Two replicates are shown. **d**, Average anteroposterior expression for genes in selected clusters, and corresponding enriched Gene Ontology (GO) terms: regulation of somitogenesis (GO 0014807); SMAD signal transduction (GO 0060395); canonical WNT signalling pathway (GO 0060070); anterior–posterior pattern specification (GO 0009952); G1–S transition of mitotic cell cycle (GO 0000082); DNA replication (GO 0006260); DNA replication initiation (GO 0006270); cellular response to interleukin 4 (IL-4) (GO 0071353); somitogenesis (GO 0001756); and Notch signalling pathway (GO 0007219). Lines, mean; shading, s.d. (Supplementary Data 3). **e**, Gene expression of characteristic markers of all three germ layers. Selected genes are highlighted (Supplementary Data 2). The colour scale corresponds to that in **c**. **f**, Localization of HOX gene expression along the anteroposterior axis. White bars indicate a lack of the paralogue in humans. $n = 2$ gastruloids (**a**–**f**). See Methods, Source Data.

Together, these observations indicate that the spatial activity of signalling molecules and subsequent patterning in human gastruloids might mirror those of mammalian embryos.

Comparative spatial transcriptomics

The high degree of organization in gene expression that we observed in human gastruloids prompted us to investigate how these patterns correspond with other developmental models. To do this, we focused on mouse gastruloids as an equivalent model system[9,10]. Comparison of mouse and human gastruloid tomo-seq datasets showed that there was a high degree of conservation in axial patterning (Fig. 4g, Supplementary Data 8). In particular, we observed a conserved pattern of mesodermal differentiation along the anterioposterior axis of the gastruloids[24]. There was a posterior-to-anterior signature of somitogenesis, with the expression of tailbud genes (*BRA*, *CDX2* and *LFNG*) posteriorly, a short domain of *MESP1* and *MESP2* expression and a more-anterior, broader domain of *MEOX1* and *TCF15* expression (Fig. 4h). The overall pattern of gene expression therefore mirrors the organization of paraxial mesoderm specification and differentiation in a mammalian embryo[25], as well as the temporal sequences of somitogenesis in human ES cells[7,26]. In contrast to these conserved patterns, we also noticed genes that were expressed in different regions (clusters 0, 2, 3 and 13 for example; Supplementary Data 8) or uniquely expressed (Extended Data Fig. 9a–e, Supplementary Data 9) in each of the two systems, supporting the notion that species-specific regulation of patterning might be occurring in the gastruloid models.

Perspectives

The human gastruloid system that we introduce here represents a first step towards the in vitro modelling of the emergence of the human body plan in a three-dimensional context. In this regard, the axial organization of the somitogenesis program of gene expression that

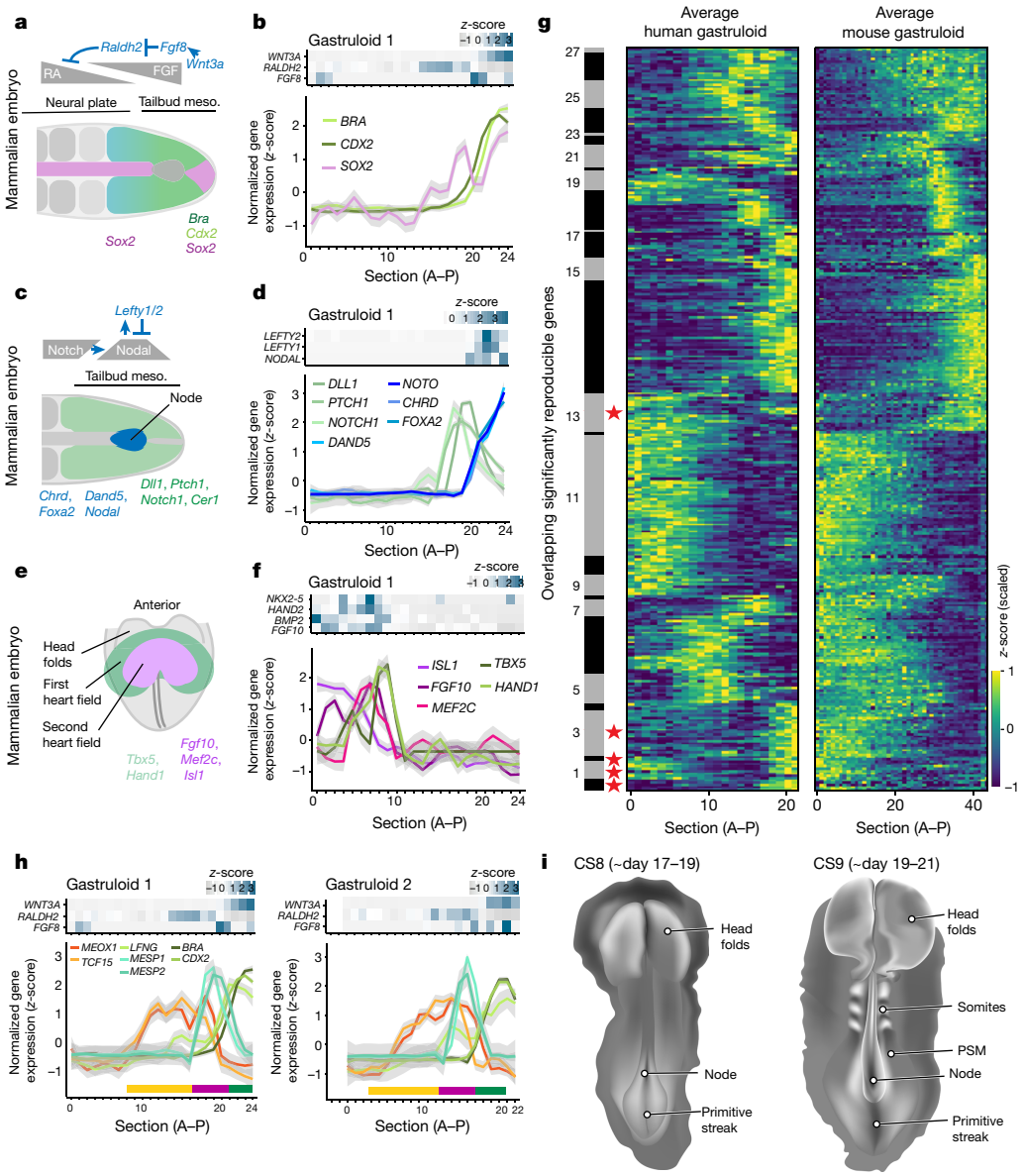

Fig. 4 | Comparative elements of early embryogenesis. a, Schematic of the tailbud of the mammalian embryo. Meso., mesoderm; RA, retinoic acid. *Raldh2* is also known as *Aldh1a2*; *Bra* is also known as *T*. **b**, Heat maps (top) and line graphs (bottom) showing the anteroposterior organization of tailbud-associated gene expression in human gastruloids. Line graphs are displayed as smoothened patterns of gene expression. Grey shading, 50% confidence interval. One replicate is shown ($n = 2$ gastruloids); see Extended Data Fig. 5c. *RALDH2* is also known as *ALDH1A2*. **c**, Schematic of the node region of the mammalian embryo. **d**, Anteroposterior organization of node-associated gene expression in human gastruloids. The panel is organized as in **b**. **e**, Schematic of the cardiac mesoderm region of the mammalian embryo. **f**, Anteroposterior organization of cardiac-mesoderm-associated gene expression in human gastruloids. The panel is organized as in **b**. **g**, Heat map showing the anteroposterior expression of 253 orthologous, reproducible genes in mouse and human gastruloids (left, average human gastruloid; right, average mouse gastruloid); 20-µm section tomo-seq data. Numbered greyscale blocks (left) show clustering based on expression patterns; red stars indicate deviation of expression pattern ($n = 2$ human gastruloids, 5 mouse gastruloids). **h**, Patterned organization of somitogenesis-related genes in human gastruloids, including signalling gradients (top heat maps), and genes related to the tailbud and somitic tissue (bottom line graphs) for $n = 2$ gastruloids. **i**, Illustration of CS8 and CS9 human embryos, showing gross anatomical features, including somite boundaries. Yellow bars, somites; magenta bars, developing somites and presomitic mesoderm (PSM); green bars, primitive streak and tailbud mesoderm; black bars, node. See Methods, Source Data.

we observed suggests an approximate staging. Images of extant collections of human embryos[3] indicate that a major transition between Carnegie stages (CS) 8 and 9 (corresponding to days 17–19 and days 19–21, respectively) is associated with the onset of somitogenesis (Fig. 4i); CS9 embryos have one to three pairs of somites that are absent in CS8 embryos. In the human gastruloids, the pattern of gene expression—with a central somitic domain and posterior presomitic domain of a similar length—leads us to suggests that 72-h human gastruloids might serve as a model for some of the features of late CS8 or early CS9 human development. With the current protocol, the majority of human gastruloids curl or retract after 72 h; this probably represents a technical limitation, and extension beyond this point will require further study.

The lack of anterior neural and extra-embryonic lineages that is characteristic of gastruloids raises important questions about the self-organization of the mammalian body plan, but also removes several

of the ethical considerations that are associated with prolonged culturing of human embryo. Human gastruloids represent an experimental model that could prove fruitful in the study of the mechanisms associated with early human development and disease, and their tractable nature should allow the detailed exploration of a variety of questions associated with human embryogenesis.

Online content

Any methods, additional references, Nature Research reporting summaries, source data, extended data, supplementary information, acknowledgements, peer review information; details of author contributions and competing interests; and statements of data and code availability are available at https://doi.org/10.1038/s41586-020-2383-9.

1. Solnica-Krezel, L. & Sepich, D. S. Gastrulation: making and shaping germ layers. *Annu. Rev. Cell Dev. Biol.* **28**, 687–717 (2012).
2. Hyun, I., Wilkerson, A. & Johnston, J. Embryology policy: revisit the 14-day rule. *Nature* **533**, 169–171 (2016).
3. O'Rahilly, R. & Müller, F. Developmental stages in human embryos (Carnegie Institution of Washington, 1987).
4. Thomson, J. A. et al. Embryonic stem cell lines derived from human blastocysts. *Science* **282**, 1145–1147 (1998).
5. Zhang, X. et al. Pax6 is a human neuroectoderm cell fate determinant. *Cell Stem Cell* **7**, 90–100 (2010).
6. Barry, C. et al. Species-specific developmental timing is maintained by pluripotent stem cells ex utero. *Dev. Biol.* **423**, 101–110 (2017).
7. Loh, K. M. et al. Mapping the pairwise choices leading from pluripotency to human bone, heart, and other mesoderm cell types. *Cell* **166**, 451–467 (2016).
8. Warmflash, A., Sorre, B., Etoc, F., Siggia, E. D. & Brivanlou, A. H. A method to recapitulate early embryonic spatial patterning in human embryonic stem cells. *Nat. Methods* **11**, 847–854 (2014).
9. Beccari, L. et al. Multi-axial self-organization properties of mouse embryonic stem cells into gastruloids. *Nature* **562**, 272–276 (2018).
10. van den Brink, S. C. et al. Symmetry breaking, germ layer specification and axial organisation in aggregates of mouse embryonic stem cells. *Development* **141**, 4231–4242 (2014).
11. Davidson, K. C. et al. Wnt/β-catenin signaling promotes differentiation, not self-renewal, of human embryonic stem cells and is repressed by Oct4. *Proc. Natl Acad. Sci. USA* **109**, 4485–4490 (2012).
12. Allison, T. F. et al. Identification and single-cell functional characterization of an endodermally biased pluripotent substate in human embryonic stem cells. *Stem Cell Reports* **10**, 1895–1907 (2018).
13. Martyn, I., Kanno, T. Y., Ruzo, A., Siggia, E. D. & Brivanlou, A. H. Self-organization of a human organizer by combined Wnt and Nodal signalling. *Nature* **558**, 132–135 (2018).
14. Massey, J. et al. Synergy with TGFβ ligands switches WNT pathway dynamics from transient to sustained during human pluripotent cell differentiation. *Proc. Natl Acad. Sci. USA* **116**, 4989–4998 (2019).
15. Piersma, A. H., Hessel, E. V. & Staal, Y. C. Retinoic acid in developmental toxicology: teratogen, morphogen and biomarker. *Reprod. Toxicol.* **72**, 53–61 (2017).
16. Junker, J. P. et al. Genome-wide RNA tomography in the zebrafish embryo. *Cell* **159**, 662–675 (2014).
17. Wymeersch, F. J. et al. Transcriptionally dynamic progenitor populations organised around a stable niche drive axial patterning. *Development* **146**, dev168161 (2019).
18. Vega-Hernández, M., Kovacs, A., De Langhe, S. & Ornitz, D. M. FGF10/FGFR2b signaling is essential for cardiac fibroblast development and growth of the myocardium. *Development* **138**, 3331–3340 (2011).
19. Watanabe, Y. et al. *Fibroblast growth factor 10* gene regulation in the second heart field by Tbx1, Nkx2-5, and Islet1 reveals a genetic switch for down-regulation in the myocardium. *Proc. Natl Acad. Sci. USA* **109**, 18273–18280 (2012).
20. Yoney, A. et al. WNT signaling memory is required for ACTIVIN to function as a morphogen in human gastruloids. *eLife* **7**, e38279 (2018).
21. Dunn, N. R., Vincent, S. D., Oxburgh, L., Robertson, E. J. & Bikoff, E. K. Combinatorial activities of Smad2 and Smad3 regulate mesoderm formation and patterning in the mouse embryo. *Development* **131**, 1717–1728 (2004).
22. Juan, H. & Hamada, H. Roles of *nodal-lefty* regulatory loops in embryonic patterning of vertebrates. *Genes Cells* **6**, 923–930 (2001).
23. Kelly, R. G., Buckingham, M. E. & Moorman, A. F. Heart fields and cardiac morphogenesis. *Cold Spring Harb. Perspect. Med.* **4**, a015750 (2014).
24. Wilson, V., Olivera-Martinez, I. & Storey, K. G. Stem cells, signals and vertebrate body axis extension. *Development* **136**, 1591–1604 (2009).
25. Koch, F. et al. Antagonistic activities of *Sox2* and *Brachyury* control the fate choice of neuro-mesodermal progenitors. *Dev. Cell* **42**, 514–526 (2017).
26. Diaz-Cuadros, M. et al. In vitro characterization of the human segmentation clock. *Nature* **580**, 113–118 (2020).

Methods

Data reporting

No statistical methods were used to predetermine sample size. The experiments were not randomized and the investigators were not blinded to allocation during experiments and outcome assessment.

Ethics statement

The human gastruloid model introduced in this study does not show any evidence of cell types associated with anterior neural fates, which would be required to form brain tissue, nor do they form extra-embryonic tissues, which would be required for implantation, or show evidence of multi-organ differentiation, which would be necessary for integrated organ system development. Notably, they lack the morphology of an early human embryo, and therefore do not manifest human organismal form. As such, they are non-intact, non-autonomous, and non-equivalent to in vivo human embryos, and do not have human organismal potential. Our research was subject to review and approval from the Human Biology Research Ethics Committee of the University of Cambridge, in compliance with the ISSCR 2016 guidelines.

Human cell lines

The cell lines used in this study include the human ES cell lines MasterShef7 (ref. [27]) S4-GATA6-GFP (ref. [12]), RUES2-GLR (ref. [13]) and RUES2-SMAD1-RFP;H2B-mCitrine (ref. [20]). All cells were cultured in humidified incubators at 37 °C and 5% CO_2. Human ES cells were cultured routinely in Nutristem hPSC XF medium (Biological Industries, 05-100-1A) on 0.5 μg cm^{-2} Vitronectin-coated plates (Gibco, A14700). Cells were passaged using 0.5 mM EDTA in phosphate-buffered saline without Mg^{2+} or Ca^{2+} ($PBS^{-/-}$) (Invitrogen, 15575-038).

Culturing human gastruloids

A critical part of the human gastruloid process is the starting state of the cells, which must be in optimal condition before beginning. When human ES cells were around 40–60% confluent, adherent cultures were pre-treated in Nutristem supplemented with CHIR99021 (Chiron; Tocris Biosciences, 4423). We found that cells did not form elongated gastruloids when cultured in an alternative pluripotency medium, including mTeSR or Essential 8. The optimal concentration of Chiron in this pre-treatment was cell-line-dependent and was determined empirically by titration for each new line. Concentrations for the lines used in this study are described in the next section ('Cell-line-dependent Chiron pulse'). After pre-treatment for 24 h, cells were dissociated using 0.5 mM EDTA in $PBS^{-/-}$ (Invitrogen, 15575-038), washed in $PBS^{-/-}$ and reaggregated in basal differentiation medium, Essential 6 (E6; Thermo Fisher Scientific, A15165-01), supplemented with 1:2,000 Y-27632 (ROCK inhibitor; Sigma Aldrich, Y0503) and a cell-line-dependent concentration of Chiron. Cell numbers were determined using an automated cell counter (Moxi Z Mini, ORFLO Technologies, MXZ002) and 400–600 cells per 40 μl were added to each well of an ultra-low-adherence 96-well plate (CellStar, 650970). For all images shown, 400 cells per well of a 96-well plate were used to generate human gastruloids, unless otherwise stated. The cell suspension was centrifuged using a bencht op plate centrifuge (Eppendorf) at 700 rpm at room temperature for 2 min. The following day, 150 μl fresh E6 medium was added to each well. The medium was exchanged for fresh E6 medium daily after this time point. Detailed instructions for generating human gastruloids can be found in Protocol Exchange[28].

Cell-line-dependent Chiron pulse

We found that different human ES cell lines required different concentrations of Chiron both before aggregation and for the first day of aggregation to generate elongating gastruloids (Extended Data Fig. 1e). The cell-line-dependent doses of Chiron used in this study were as follows: RUES2-GLR, 3.25 μM Chiron pre-treatment, 0.5 μM Chiron aggregation; MasterShef7, 5 μM Chiron pre-treatment, 3 μM Chiron aggregation; S4-GATA6-GFP, 3.25 μM Chiron pre-treatment, 0.5 μM Chiron aggregation; RUES2-SMAD1-RFP;H2B-mCitrine, 5 μM Chiron pre-treatment, 3 μM Chiron aggregation.

Signal modulation experiments

RUES2-GLR cells were pre-treated for one day in Nutristem supplemented with 100 ng ml^{-1} recombinant human WNT3A (5036-WN-010) or 50 ng ml^{-1} BMP4 (314-BP), and aggregated in E6 and ROCK inhibitor with additional supplementation as shown. Subsequent medium changes were performed daily with E6 alone. To further test the effect of signal modulation on gastruloid formation, RUES2-GLR cells were pre-treated in Nutristem supplemented with 3.25 μM Chiron and one of 1 μM LDN193189 (04-0074), 1 μM XAV-939 (04-0046) or 10 μM SB431542 (1614) before aggregation in E6 with 0.5 μM Chiron and ROCK inhibitor, unless otherwise stated. Subsequent medium changes were performed daily with E6 alone. For retinoic acid experiments, RUES2-GLR cells were pre-treated as usual in 3.25 μM Chiron for 1 day, before aggregation in E6 supplemented with 0.5 μM Chiron, ROCK inhibitor and 0.5 μM retinoic acid (R2625). Subsequent medium changes were performed daily with E6 and 0.5 μM retinoic acid.

The SB43 pre-treated gastruloids for tomo-seq were made with RUES2-GLR cells pre-treated in Nutristem with 3.25 μM Chiron and 10 μM SB431542 (1614). They were then aggregated in E6 with 3 μM Chiron and ROCK inhibitor. Subsequent medium changes were performed daily with E6 alone.

Scanning electron microscopy

Human gastruloids, made from the RUES2-GLR line at 72 h after aggregation, were washed twice with HEPES buffer and fixed overnight in 3% glutaraldehyde, 0.05 M sodium cacodylate buffer pH 7.4 at 4 °C. Samples were washed several times in deionized water (DIW) at room temperature to remove fixative. Melinex coverslips at 12-mm diameter were covered with a large drop of poly-L-lysine solution (Sigma P4707) and incubated for 15 min at room temperature. Excess solution was drained off and the coverslips were allowed to air-dry at 37 °C. The gastruloids were transferred to the poly-L-lysine coated coverslips in a drop of DIW and allowed to adhere for about 30 min at room temperature while ensuring that the gastruloids remained covered with DIW. Excess DIW was carefully drained off using a tissue paper and the samples were immediately plunge-frozen in liquid-nitrogen-cooled ethane. After freeze-drying overnight in a liquid-nitrogen-cooled turbo freeze drier (Quorum Emitech K775X), samples were mounted on aluminium scanning electron microscopy stubs using sticky carbon pads and sputter-coated with 35-nm gold followed by 15-nm iridium. Samples were viewed in a FEI Verios 460 scanning electron microscope using an Everhart-Thornley detector in secondary electron mode with an accelerating voltage of 2 keV and probe current of 25 pA.

Immunostaining

Human gastruloids were fixed and immunostained according to the existing methods for gastruloid staining[29] unless otherwise stated. The antibodies used were: 1:200 rabbit anti-CDX2 (Thermo Fisher Scientific, EPR2764Y); 1:200 goat anti-GATA6 (R&D Systems, AF1700); 1:200 rabbit anti-Brachyury (AbCam, ab209665); 1:200 goat anti-SOX2 (R&D Systems, AF2018); 1:200 mouse anti-CDH2 (BD Biosciences, BD10920); 1:200 rat anti-CDH1 (Takara, M108), 1:100 rabbit anti-WNT3A (ab219412), 1:200 rabbit anti-LEF1 (ab137872) and 1:200 rabbit anti-FOXA2 (ab108422). All secondary antibodies were diluted 1:500, and included Alexa Fluor 488-, 568- and 647-conjugated antibodies (Invitrogen).

Adherent cell staining was done using 1:200 mouse anti-CDH2 (BD Biosciences, BD10920), 1:200 rat anti-CDH1 (Takara, M108) and 1:200 rabbit anti-Brachyury (AbCam, ab209665) primary antibodies.

Quantification was performed using Fiji software on the whole image (histograms) or using a line region of interest (ROI) through the colony (line graph).

In situ hybridization

Human gastruloids were collected at 72 h or 96 h post-aggregation. After rinsing them briefly in PBS, they were fixed in 4% paraformaldehyde (PFA) either overnight or for 2 h at 4 °C and stored in 100% methanol at 20 °C until further use. In situ hybridization was performed on whole mount gastruloids as described[9] with minor modifications. Gastruloids were rehydrated by incubating them for 3–5 min in a series of decreasing concentrations of methanol (75%, 50%, 25% and 0% respectively) in TBST (20 mM Tris 137 mM NaCl, 2.7 mM KCl and 0.1% Tween, pH 7.4). After washing gastruloids in TBST, they were incubated in proteinase K (2.5μg ml^{-1}) for 2 min to make them permeable to probes and post-fixed in 4% PFA for 20 min at room temperature, before washing again in TBST. To block non-specific interactions, they were pre-hybridized at 68 °C for 4–5 h. Hybridization was performed by incubating them in 200 ng ml^{-1} of specific digoxigenin (DIG)-labelled RNA probes at 68 °C overnight. The probe sequences used are provided in Supplementary Table 2. The following day, after washing the gastruloids at 68 °C, they were incubated in blocking solution for 1.5 h at room temperature. Gastruloids were then incubated overnight in anti-DIG antibody coupled to alkaline phosphatase (Sigma) at 1:3,000 dilution in blocking buffer at 4 °C. The next day, they were washed in MABT (100 mM maleic acid, 150 mM NaCl and 0.1% Tween, pH 7.5) overnight at 4 °C. Gastruloids were then washed three times with TBST and three times with alkaline phosphatase buffer (0.1 M Tris pH 9.5, 100 mM NaCl and 0.1% Tween) and incubated in BM purple solution (Sigma) either at 4 °C or room temperature until the signal was fully developed. Gastruloids were washed in TBST and post-fixed in 4% PFA for 20 min at room temperature. For imaging, gastruloids were suspended in CUBIC-R1A tissue-clearing reagent[30,31].

Quantitative PCR with reverse transcription

Gene expression was analysed from adherent cells using Trizol (Ambion LifeTechnologies) according to the manufacturer's instructions. Total RNA was quantified using a NanoDrop 2000C (Thermo Fisher Scientific) and 5 μg was added to a reverse transcription reaction with Superscript III (Invitrogen) according to the manufacturer's instructions. The resultant cDNA was quantified by quantitative PCR with SYBRGreen (Merck) using a liquid handling robot (Qiagility, Qiagen) and analysed on a RotorGeneQ thermocycler (Qiagen). Primer sequences are provided in Supplementary Table 1. The concentration of cDNA was estimated using an in-house MAK2 analysis method, as described previously[32].

Imaging

Confocal imaging was performed using a LSM700 (Zeiss) on a Zeiss Axiovert 200 M using a 40 EC Plan-NeoFluar 1.3 NA DIC oil-immersion objective. Image capture was performed using Zen2010 v6 (Carl Zeiss Microscopy). All samples were fixed and immunostained before imaging. For gastruloids made from the RUES2-GLR reporter line, we never observed a fluorescent signal of reporter proteins after our fixation protocol, and therefore used the same antibody design and microscope settings as described.

Wide-field imaging was performed using a 37 °C incubated chamber supplied with 5% CO_2, attached to a Zeiss AxioObserver.Z1 (Carl Zeiss Microscopy) as described previously[33]. All images were analysed using Fiji software[34], and any adjustments are always consistent within a panel. The presented images have been rotated to align their anteroposterior axis horizontally where necessary, as indicated by a dark grey background.

Image analysis

Germ-layer patterning. Human gastruloids made using the RUES2-GLR reporter line were specifically analysed for dynamic reporter expression. An in-house MATLAB script was developed to assess the dynamic fluorescent marker expression along the anteroposterior axis of human gastruloids. Wide-field images of gastruloids were taken at 24 h, 48 h and 72 h and aligned along their anteroposterior axis with reference to fluorescent reporter expression. For each sample, a binary image was generated in the bright-field channel and used as a mask for all fluorescent channels and the major (length) axis was identified. Consequently, for every pixel along the length axis, the sum of intensity values of the respective channel along the width of the aggregate was divided by the width of the gastruloid at that specific point, yielding the normalized fluorescence intensity along the length of the sample. This process was then repeated for every acquired fluorescent channel. Gastruloids used for this analysis were a full set from one experimental batch, and images were only excluded from the analysis when anteroposterior alignment or binarization were unsuccessful or empty wells were observed.

Elongation quantification. To quantify the degree of elongation of human gastruloids, bright-field channel wide-field images were imported into Fiji[34]. The length of the longest axis was measured using the line tool, followed by the length of the perpendicular axis at the midpoint of the longest axis line. The ratio of these two values was calculated and plotted by time point and condition, using R. Significance was assessed using the Welch two-sample *t*-test. This method was used to assess the difference in elongation with and without Chiron pre-treatment, as shown in Fig. 1d.

Morphological quantification. The proportions of gastruloid shapes (spherical, ovoid, elongated (short) and elongated (long)) were estimated for multiple independent biological replicates. This was performed using an in-house method derived from that previously described[33]. In brief, images were converted into single-channel, 8-bit TIFF files using Fiji[34]. These were then processed using Python 3.6 (Python Software Foundation, https://www.python.org/) and the Open-CV package[35] to apply a Gaussian blur before performing Otsu's thresholding and flood filling with erosion to assign a mask around the shape of each gastruloid. The length and width values were calculated using a rotated bounding box (minAreaRect), which identifies and measures the orthogonally widest and longest parts of the gastruloid. Various additional quantitative features were then extracted from the contours, which were further processed using R. The categories of each shape descriptor were defined as follows: spherical, circularity less than or equal to 1.1 or maximum width: maximum length (WL) greater than or equal to 0.95; ovoid, circularity less than or equal to 1.2 or WL greater than or equal to 0.9; elongated (short), circularity greater than 1.2 and less than or equal to 1.4 and WL less than 0.9; elongated (long), circularity less than 1.4 and WL less than 0.9. Images were quality controlled for empty wells or those with debris that compromised shape descriptors, using quantification of area or circularity outliers and confirmed manually by examination of images. This method was used to assess the reproducibility of human gastruloid experiments, as shown in Fig. 1e and Extended Data Fig. 1d.

Estimates of cell number. The number of cells per aggregate was estimated using Imaris software (Bitplane) on confocal images stained with Hoechst. Spots were drawn using the internal algorithm, using an estimated *xy* size of 6 μm, a quality threshold of 2.5 and background subtraction. Because the light penetration only allowed us to image part of the gastruloid we assumed this was on average half of the gastruloid, and so doubled the resultant estimate for the number of nuclei. It is likely that this process slightly underestimates the number of nuclei. The quantitative data were subsequently analysed in R. The

fitting of an exponential curve was done using the lm() function of log-transformed data.

Subcellular localization of SMAD1–RFP. To quantify the level of active SMAD1 in each cell of the gastruloid, we sought to determine the nuclear-to-cytoplasmic ratio of SMAD1–RFP. To do this, we used Imaris software to identify nuclear positions by creating a surface using the Hoechst channel. We then used these surfaces to create two masks: one in which everything inside the nuclear mask was set to zero, and one in which everything outside the nuclear mask was set to zero. This allowed us to distinguish the nuclear and cytoplasmic components of the SMAD1–RFP signal. To assign the cytoplasmic component to each individual cell, we used Imaris to create Spots using the Hoechst channel (estimated *xy* diameter of 5.25 µm). These were then processed using 'Spots to Spots Nearest Neighbour Distance' to create maximal cell areas relative to their neighbours. We then used these distance spots to assess the internal nuclear and cytoplasmic component of SMAD1–RFP in each cell along the anteroposterior axis.

The data were subsequently analysed in R, by normalizing the mean intensity of the nuclear SMAD1–RFP component to the mean intensity of the H2B–mCitrine value, to account for depth bias. This normalized SMAD1–RFP intensity was then divided by the mean intensity of the cytoplasmic SMAD1–RFP, to get the normalized nuclear:cytoplasmic SMAD1–RFP values.

Axial patterning quantification. RUES2-GLR gastruloids were fixed at 24 h, 48 h and 72 h time points, stained for GATA6 and CDX2 and imaged on a confocal microscope. Maximum projection images were generated using Imaris software, and nuclei were identified with Imaris using Hoechst staining (estimated *xy* size of 6 µm and quality threshold of 2.5). For each nuclear spot, the mean intensity of GATA6 and CDX2 fluorescence was acquired and plotted using R. Axial patterning was determined in Fiji using the segmented line tool with width 80 and the plotprofile tool. For each gastruloid, the anteroposterior axis was normalized between 0 and 1, and the fluorescence intensities were also scaled between 0 and 1 for the minimum and maximum values, to aid comparison between gastruloids. The aspect ratio of these gastruloids was calculated manually in Fiji using the line tool, in which the length of the perpendicular axis at the midpoint of the longest axis line was defined as the width. Three categories, with cut-offs of <2.0, >2.0 and <2.4, and >2.4, corresponded to the observed longest elongation at 24 h, 48 h, and 72 h, respectively. This method was used for quantifying elongation in confocal images, as shown in Extended Data Fig. 3e, f.

Tomo-seq and mapping

Tomo-seq was performed using an updated version of published methods[16,36] and analysed with methods described previously[37]. In brief, gastruloids were sectioned along their anteroposterior axis, and the mRNA content of each section was extracted using SORT-seq[38]. Paired end (75-bp) sequencing was performed on the resulting RNA-sequencing libraries using the Illumina NextSeq sequencing platform. Read 1 contains the section barcode and the unique molecular identifier (UMI). Read 2 contains the biological information. Reads 2 with a valid section barcode were selected and mapped using STAR v.2.5.3a with default parameters to the human GRCh38 genome (ENSEMBL version 93), and only reads mapping to gene bodies (exons) were used for downstream analysis. Reads mapping simultaneously to an exon and to an intron were assigned to the exon. Mappabilities for the different samples range between 44% and 47%. For each section, the number of transcripts was obtained as previously described[39]. We refer to transcripts as unique molecules on the basis of UMI correction.

After mapping, spike-ins, ribosomal and mitochondrial genes were removed from downstream analysis, together with *KCNQ1OT1*, *LARS2* and *MALAT1*, because these genes seem to be linked to mapping errors and have been shown to be erroneous in previous studies.

In each gastruloid, the data were then normalized to the median number of unique transcripts per slice, and the *z*-score of each gene was extracted along sections.

Gene expression data analysis

The reproducibility of the anteroposterior expression pattern between different gastruloid replicates was scored for each gene using a random background model to calculate the Pearson correlation coefficient *P* value[37]. The *P* value threshold to select reproducible genes was set at 0.001. These significantly reproducible genes were then clustered using a self-organizing map (SOM) method, followed by hierarchical clustering to determine general patterns of gene expression along the anteroposterior axis.

Average gastruloid profiles were generated using the mean *z*-scores along the anteroposterior axis. When the number of sections between replicates was different, values were quadratically interpolated to fill spaces using the interp1d function from the package scipy.interpolate (Python v.3.6).

Differential gene expression was performed by normalizing the transcripts in each section to 100,000 for all gastruloids, then pooling all sections of each gastruloid together and finally assessing significant differentially expressed genes on the basis of total expression using the binomial test.

For smoothened line graphs of gene expression, the distribution of gene expression along the sections was plotted using R, and smoothened using the geom_smooth() function (method = loess, span = 0.3, level = 0.5) to minimize background variability. For each gene expression distribution, the confidence interval is therefore shown (at 0.5 confidence interval) as a grey ribbon.

Gene Ontology term analysis for each hierarchical cluster of the human gastruloids that were pre-treated with Chiron was performed using ENSEMBL IDs run with the DAVID Annotation tool[40] with the human genome as a background model, focusing on biological process terms. Statistical correction for multiple comparisons was achieved using Benjamini adjustment.

Gene Ontology for each hierarchical cluster of the human-to-mouse gastruloid comparison was performed using the Python package GOATOOLS[41], which uses Fisher's exact test, setting the *P* value at 0.05. The list of reproducible genes in each corresponding condition or the full human transcriptome was set as a background model, focusing on biological process terms. Statistical correction for multiple comparisons was achieved using Bonferroni adjustment.

Mouse gastruloid comparison

We compared 72-h human gastruloids, which we believe correspond approximately to the CS9 human embryo, with 120-h mouse gastruloids, which are thought to represent a mouse embryo at the embryonic day (E) 8–E8.5 stage, an approximately equivalent developmental stage[42]. These mouse gastruloids were generated from the LfngT2AVenus line[43]. Full details of this dataset can be found in a previous study[37].

A gene reproducibility analysis between the replicates of mouse gastruloids (*P* value < 0.01) and the two replicates of human gastruloids (*P* value < 0.001) was performed, independently (as described above). Only genes present in the two separate lists that had human–mouse orthologues were used for downstream analysis. The list of human–mouse orthologues was obtained from Biomart, Ensembl 93. Genes were clustered on the basis of their anteroposterior expression pattern in both the mouse and the human average gastruloid simultaneously, as described above. The Pearson correlation coefficient for each gene was calculated between the anteroposterior expression pattern of two different samples (in *z*-score units). To assess for significantly correlated genes, we randomly generated 10,000 expression profiles with the same number of sections as in the pair of replicates and determined the correlation value at which fewer than 100 random profiles have larger correlation values (*P* value < 0.01).

Reporting summary

Further information on research design is available in the Nature Research Reporting Summary linked to this paper.

Data availability

All RNA-sequencing datasets produced in this study are deposited in the Gene Expression Omnibus (GEO) under accession code GSE123187. Source data are provided with this paper.

Code availability

Code is available at https://github.com/vikas-trivedi/Human-Gastruloids_Fluorescence, https://github.com/anna-alemany/humanGastruloids_tomoseq and https://github.com/naomi-moris/humanGastruloids_shapeDescriptors.

27. Canham, M. A. et al. The molecular karyotype of 25 clinical-grade human embryonic stem cell lines. *Sci. Rep*. **5**, 17258 (2015).
28. Moris, N. et al. Generating human gastruloids from human embryonic stem cells. *Protoc. Exch*. https://doi.org/10.21203/rs.3.pex-812/v1 (2020).
29. Baillie-Johnson, P., van den Brink, S. C., Balayo, T., Turner, D. A. & Martinez Arias, A. Generation of aggregates of mouse embryonic stem cells that show symmetry breaking, polarization and emergent collective behaviour in vitro. *J. Vis. Exp*. **105**, e53252 (2015).
30. Susaki, E. A. et al. Whole-brain imaging with single-cell resolution using chemical cocktails and computational analysis. *Cell* **157**, 726–739 (2014).
31. Susaki, E. A. et al. Advanced CUBIC protocols for whole-brain and whole-body clearing and imaging. *Nat. Protoc*. **10**, 1709–1727 (2015).
32. Turner, D. A. et al. Wnt/β-catenin and FGF signalling direct the specification and maintenance of a neuromesodermal axial progenitor in ensembles of mouse embryonic stem cells. *Development* **141**, 4243–4253 (2014).
33. Turner, D. A. et al. Anteroposterior polarity and elongation in the absence of extra-embryonic tissues and of spatially localised signalling in gastruloids: mammalian embryonic organoids. *Development* **144**, 3894–3906 (2017).
34. Schindelin, J. et al. Fiji: an open-source platform for biological-image analysis. *Nat. Methods* **9**, 676–682 (2012).
35. Bradski, G. The OpenCV library. *Dr. Dobb's: The World of Software Development* https://www.drdobbs.com/open-source/the-opencv-library/184404319 (2000).
36. Kruse, F., Junker, J. P., van Oudenaarden, A. & Bakkers, J. *Tomo*-seq: a method to obtain genome-wide expression data with spatial resolution. *Methods Cell Biol*. **135**, 299–307 (2016).
37. van den Brink, S. C. et al. Single-cell and spatial transcriptomics reveal somitogenesis in gastruloids. *Nature* (2020).
38. Muraro, M. J. et al. A single-cell transcriptome atlas of the human pancreas. *Cell Syst*. **3**, 385–394 (2016).
39. Grün, D., Kester, L. & van Oudenaarden, A. Validation of noise models for single-cell transcriptomics. *Nat. Methods* **11**, 637–640 (2014).
40. Huang, W., Sherman, B. T. & Lempicki, R. A. Systematic and integrative analysis of large gene lists using DAVID bioinformatics resources. *Nat. Protoc*. **4**, 44–57 (2009).
41. Klopfenstein, D. V. et al. GOATOOLS: a Python library for gene ontology analyses. *Sci. Rep*. **8**, 10872 (2018).
42. Theiler, K. *The House Mouse: Atlas of Embryonic Development* 2nd edn (Springer-Verlag, 1989).
43. Sonnen, K. F. et al. Modulation of phase shift between Wnt and Notch signalling oscillations controls mesoderm segmentation. *Cell* **172**, 1079–1090 (2018).

Acknowledgements We thank V. Trivedi for his help writing the dynamic fluorescent reporter analysis code; D. Turner and A. Baranowski for their help developing the image analysis code; K. Muller from the Cambridge Advance Imaging Centre (CAIC) for help with scanning electron microscopy; the Utrecht Sequencing Facility for sequencing; A. Ebbing, J. Vivié and M. Betist for the robotized tomo-seq protocol; and members of the Martinez Arias and van Oudenaarden laboratories, as well as B. Steventon, P. Rugg-Gunn, M. Lütolf, M. Johnson and N. Hopwood, for discussions over the course of this work. This work was supported by funds from the Newton Trust (INT16.24b), Leverhulme Trust (RPG-2018-356) and MRC (MR/R017190/1) to A.M.A., N.M., S.G. and T.B. and a European Research Council Advanced Grant (ERC-AdG 742225-IntScOmics), a Nederlandse Organisatie voor Wetenschappelijk Onderzoek (NWO) TOP award (NWO-CW 714.016.001) and the Foundation for Fundamental Research on Matter, financially supported by NWO (FOM-14NOISE01), to S.C.v.d.B., A.A. and A.v.O. This work is part of the Oncode Institute, which is partly financed by the Dutch Cancer Society. It was also supported by a Constance Work Junior Research Fellowship from Newnham College, Cambridge to N.M. and an Erasmus+ grant to K.A. and J.S.

Author contributions N.M. and K.A. designed, optimized and performed the human gastruloid experiments, with help from T.B. and A.M.A., and the A.v.O. laboratory independently replicated the entire process. N.M. and S.C.v.d.B. embedded the human gastruloids and S.C.v.d.B. performed sectioning and tomo-seq preparation. A.A. analysed transcriptomic datasets, with analysis input from N.M., S.C.v.d.B., A.v.O. and A.M.A. N.M. created embryonic illustrations. J.S. designed and made in situ probes and J.S. and S.G. performed in situ hybridizations. A.M.A. and A.v.O. supervised research. N.M and A.M.A. wrote the manuscript with considerable input from all authors. All authors reviewed the manuscript.

Competing interests This work is the subject of a patent application (PCT/GB2019/052670) filed by Cambridge Enterprise on behalf of the University of Cambridge (international filing date 23/09/2019; published 26/03/2020), covering the generation and use of human gastruloids. The inventors are N.M. and A.M.A. The remaining authors declare no competing interests.

Additional information

Supplementary information is available for this paper at https://doi.org/10.1038/s41586-020-2383-9.

Correspondence and requests for materials should be addressed to N.M., A.v.O. or A.M.A.

Peer review information *Nature* thanks Jianping Fu and the other, anonymous, reviewer(s) for their contribution to the peer review of this work.

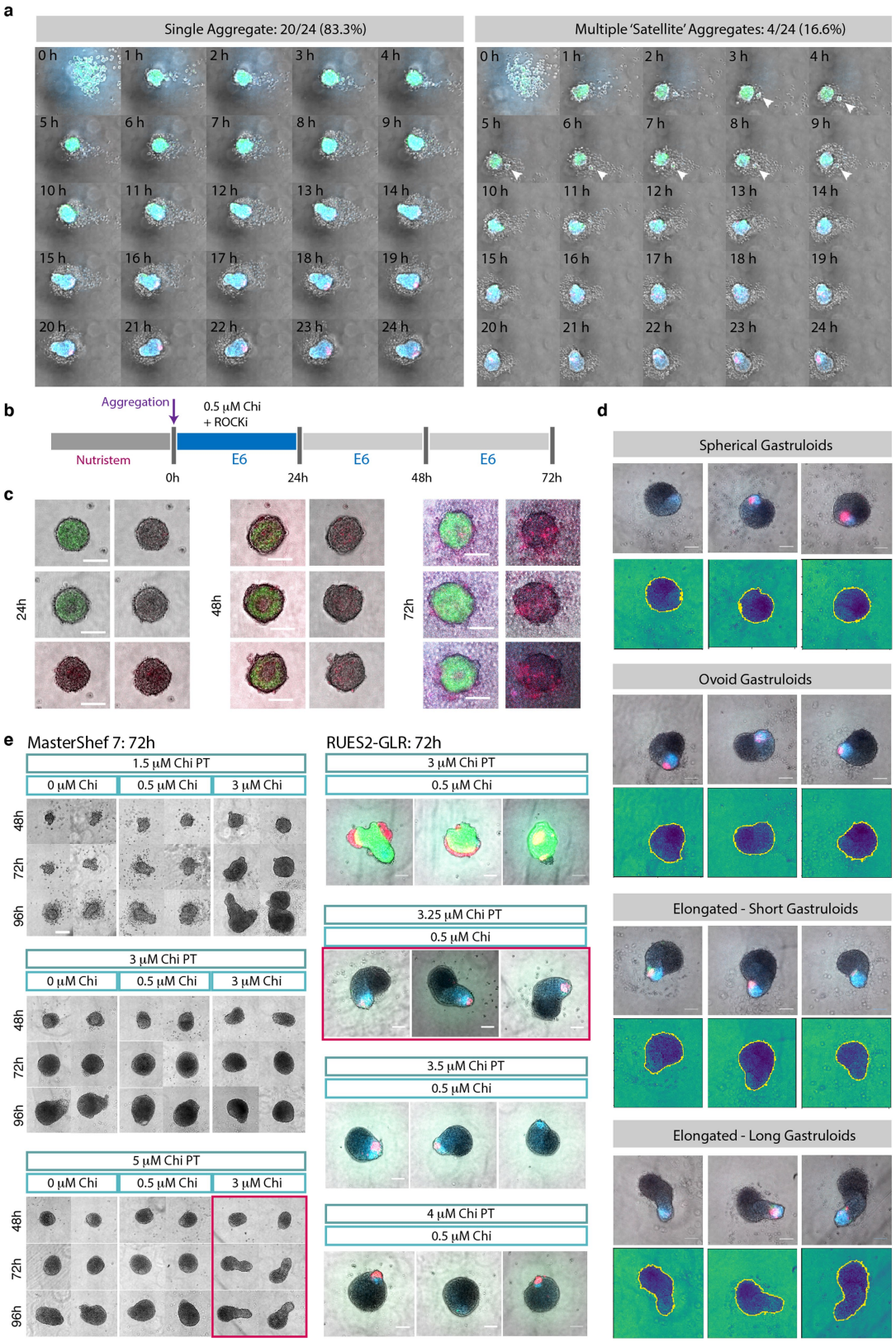

Extended Data Fig. 1 | See next page for caption.

Extended Data Fig. 1 | Optimization of the Chiron pre-treatment and morphological variability. a, Aggregation of single RUES2-GLR cells after pre-treatment with Chiron, showing either a single aggregate (left) or the presence of transient 'satellite' aggregates (right). These typically merge within 10 h ($n = 38$ gastruloids from $n = 2$ experiments). **b**, Schematic of the protocol without Chiron pre-treatment, but with aggregation in Chiron and ROCK inhibitor medium. **c**, Gastruloids made from the RUES2-GLR line without Chiron pre-treatment at 24 h, 48 h and 72 h after aggregation. Three examples are shown that are representative of five independent experiments for each time point ($n = 415$ gastruloids), with all three fluorescent reporters (SOX2–mCitrine, SOX17–tdTomato and BRA–mCerulean; left) and without SOX2–mCitrine (right). Scale bars, 100 µm. **d**, Examples of reporter patterning in differential morphological classes, as assessed by automated segmentation providing gastruloid outline boundaries (yellow line indicates the boundary used for quantifications). Three gastruloids per category are shown that are representative of seven independent experiments ($n = 374$ gastruloids). See Methods for details of the classification method. Scale bars, 100 µm. **e**, Cell-line-dependent optimization of Chiron conditions. Human gastruloids were derived from the MasterShef7 cell line (left; two examples shown) or the RUES2-GLR cell line (right; three examples shown). Red boxes indicate the concentrations at which gastruloids were deemed to be optimally elongated, and the resultant conditions for subsequent gastruloid derivation. Representative examples are shown from three independent experiments. Scale bars, 100 µm.

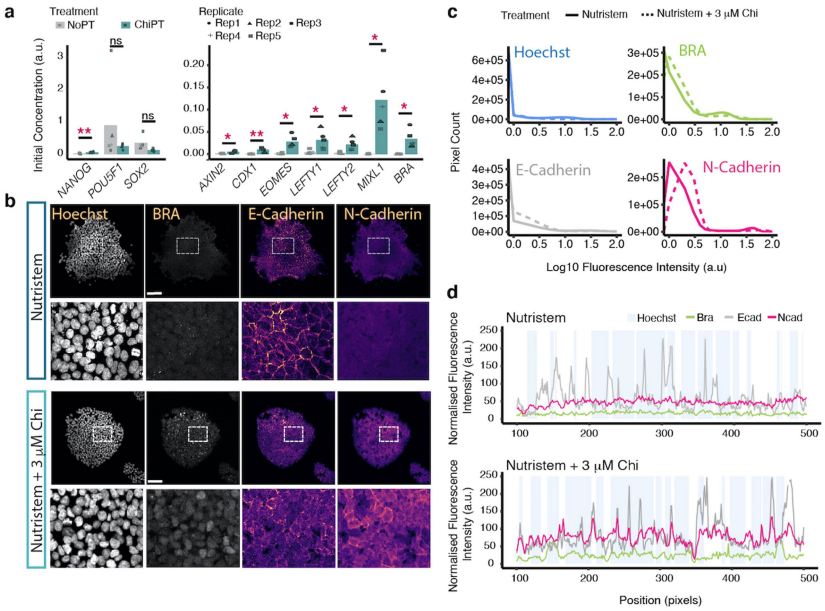

Extended Data Fig. 2 | Effect of Chiron pre-treatment on human ES cells. **a**, Gene expression in adherent RUES2-GLR cells after 24 h of Chiron pre-treatment (ChiPT) compared to cells that were not pre-treated (Nutristem alone; NoPT), as assessed by quantitative PCR with reverse transcription. Averages from five biological replicates are shown; bars, mean average; points, technical averages for each experimental replicate. $^{*}P < 0.05$, $^{**}P < 0.01$, NS, not significant ($P > 0.05$) (Welch two-sided, two-sample *t*-test). See Methods, Source Data. **b**, Immunostaining of adherent colonies of RUES2-GLR cells that were not pre-treated (top) or that were pre-treated with Chiron for 24 h (bottom) for Brachyury (BRA), E-cadherin and N-cadherin. Dashed boxes show the position of enlarged regions. One representative example is shown from two independent experiments. Scale bars, 100 μm. **c**, Quantified expression from immunostaining of RUES2-GLR cells as shown in **b**. The whole image was used to generate these data. **d**, Profiles of membrane localization of E-cadherin and N-cadherin from immunostaining of RUES2-GLR cells as shown in **b**.

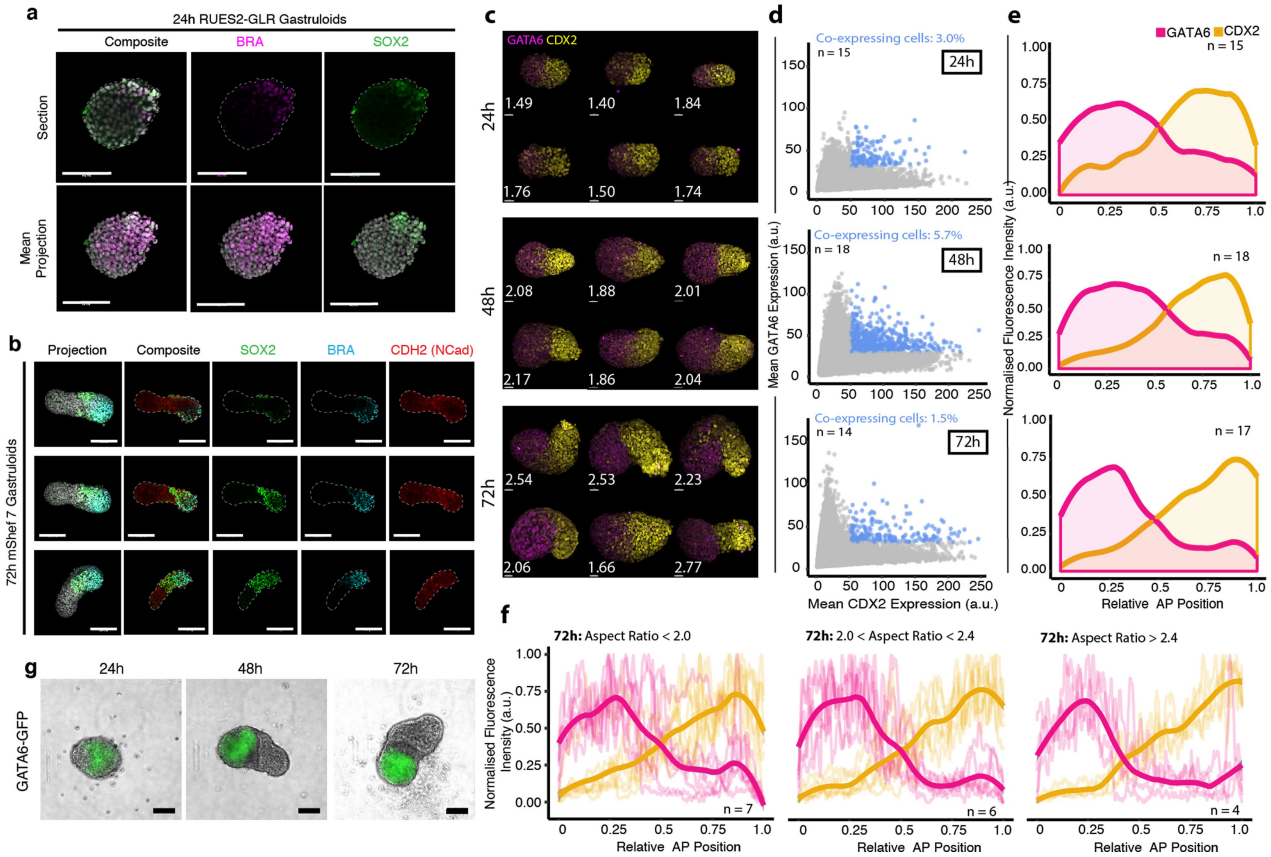

Extended Data Fig. 3 | Establishing axial patterning in human gastruloids. **a**, Immunofluorescence imaging of a RUES2-GLR human gastruloid at 24 h. Confocal sections (top) and mean projection (bottom) of the gastruloid. One representative example is shown from two experiments ($n = 12$ gastruloids). Scale bars, 100 µm. **b**, MasterShef7 human gastruloids at 72 h after aggregation, showing BRA, SOX2 and N-cadherin (CDH2) localization. Three representative examples are shown, from three experiments ($n = 13$ gastruloids). Scale bars, 100 µm. **c**, Projection of immunofluorescently labelled RUES2-GLR human gastruloids at 24 h, 48 h and 72 h with GATA6 (magenta) and CDX2 (yellow) staining. Six representative gastruloids are shown for each time point. Numbers, aspect ratio. Representative examples are shown from two independent experiments ($n = 63$ gastruloids). Scale bars, 30 µm. **d**, Scatter plot of the co-expression of GATA6 and CDX2 per cell, across the three time points. Blue points, co-expression over threshold; grey points, expression below threshold. The number of gastruloids in each plot is shown (n). **e**, Relative axial expression of GATA6 (magenta) and CDX2 (yellow) along the anteroposterior axis. The number of gastruloids in each plot is shown (n). **f**, Relative axial expression of GATA6 (magenta) and CDX2 (yellow) along the anteroposterior axis, stratified by aspect ratio (as determined using a manual axial patterning quantification; see Methods for details). Thick lines, mean; thin lines, individual gastruloids. The number of gastruloids in each plot is shown (n). Representative images of gastruloid elongation classifications are shown in **c**. **g**, Progressive polarization and restriction of GATA6–GFP fluorescence to the anterior pole of S4-GATA6-GFP human gastruloids. One representative example is shown ($n = 17$ gastruloids). Scale bars, 100 µm.

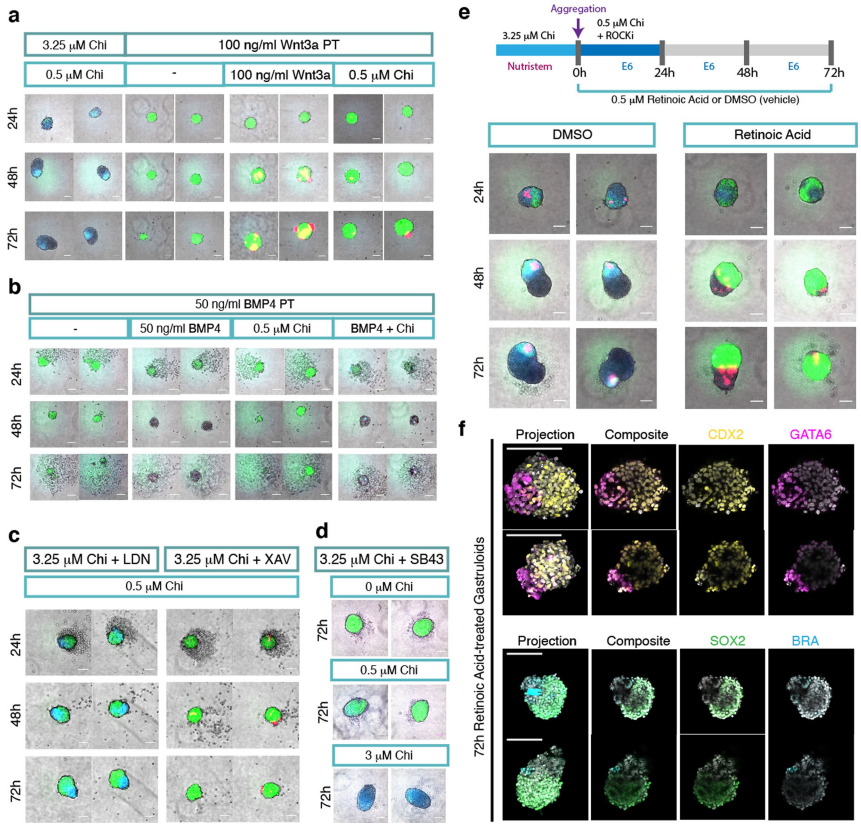

Extended Data Fig. 4 | Disrupting axial patterning in human gastruloids. **a**, RUES2-GLR cell aggregates after pre-treatment (PT) with WNT3A instead of Chiron for 24 h. Representative examples are shown ($n = 281$ gastruloids). **b**, RUES2-GLR cell aggregates after pre-treatment with BMP4 for 24 h. Representative examples are shown ($n = 187$ gastruloids). **c**, Application of a BMP inhibitor, LDN193189 (LDN; left) or tankyrase inhibitor, XAV-939 (XAV; right) during 24-h pre-treatment of RUES2-GLR cells. Representative examples are shown ($n = 85$ gastruloids). **d**, Application of a Nodal signalling inhibitor, SB43 (SB43) during 24-h pre-treatment of RUES2-GLR cells. **a**–**d**, Two representative examples are shown for each condition (three independent experiments). Dark green boxes indicate pre-treatment in Nutristem; teal boxes indicate the aggregation medium composition (E6 and ROCK inhibitor). Scale bars, 100 μm. **e**, Addition of retinoid acid (right) or DMSO (left) to RUES2-GLR human gastruloids for each day of aggregate development. Schematic of the protocol (top) and imaging results (bottom). See Methods for experimental details. Representative examples are shown from four independent experiments ($n = 159$ gastruloids). Scale bars, 100 μm. **f**, Confocal imaging of axial patterning defects in 72-h RUES2-GLR human gastruloids treated with retinoic acid. Representative examples are shown from three independent experiments ($n = 25$ gastruloids). Scale bars, 100 μm.

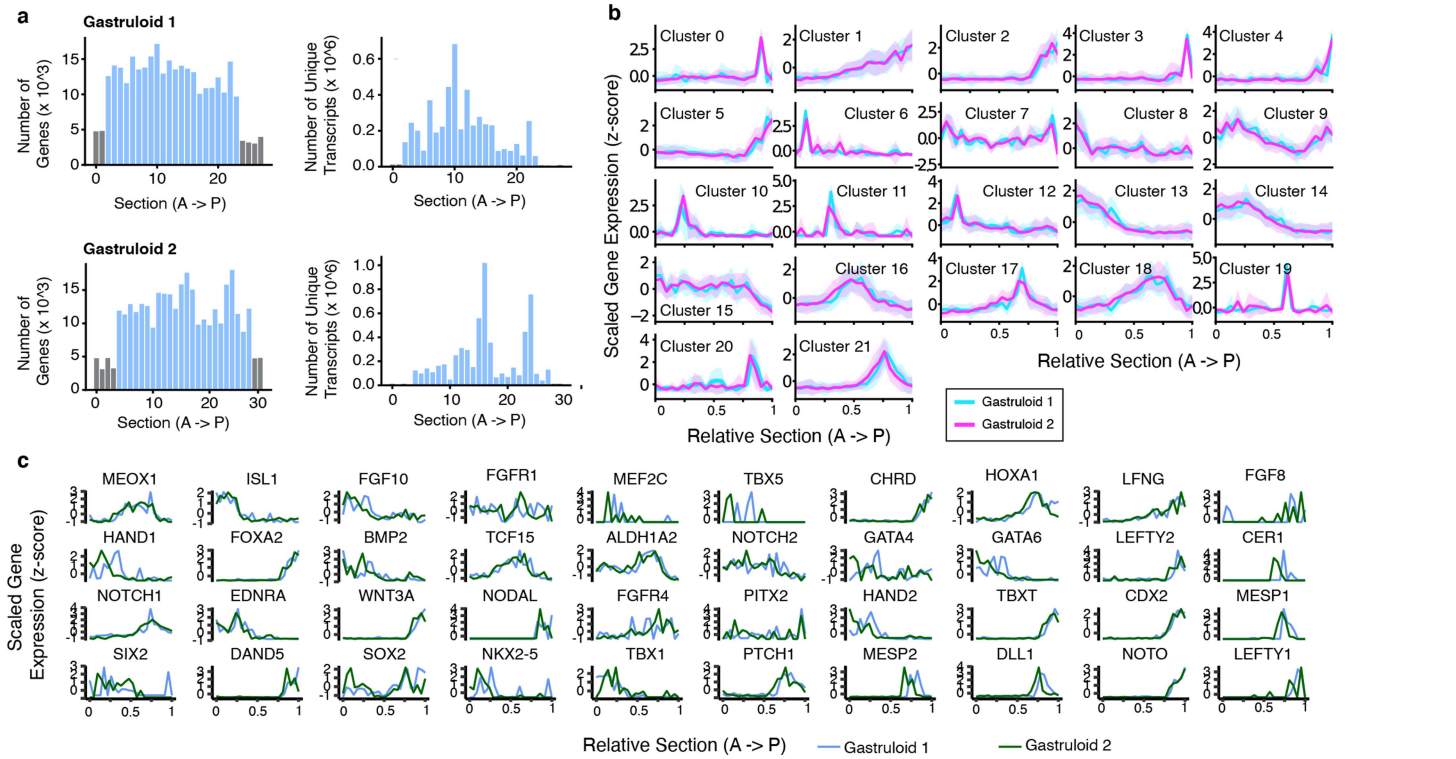

Extended Data Fig. 5 | Spatial transcriptomics by tomo-seq identifies clusters of gene expression. a, Quantification of the number of genes (left) and number of unique transcripts (right) detectable in each section along the anteroposterior axis of 72-h RUES2-GLR human gastruloids pre-treated with Chiron. Blue bars, sections above the threshold used for downstream tomo-seq analysis; grey bars, sections below the threshold (see Methods for details). Two replicates are shown. **b**, Average expression patterns along the anteroposterior axis of all genes detected in each cluster. Clusters correspond to those in Fig. 3c and Supplementary Data 1. Lines, mean; shading, s.d. for the set of genes within each cluster ($n = 2$ gastruloids). **c**, Selection of gene traces along the anteroposterior axis for both gastruloids. Blue and green lines, expression values for replicates 1 and 2, respectively.

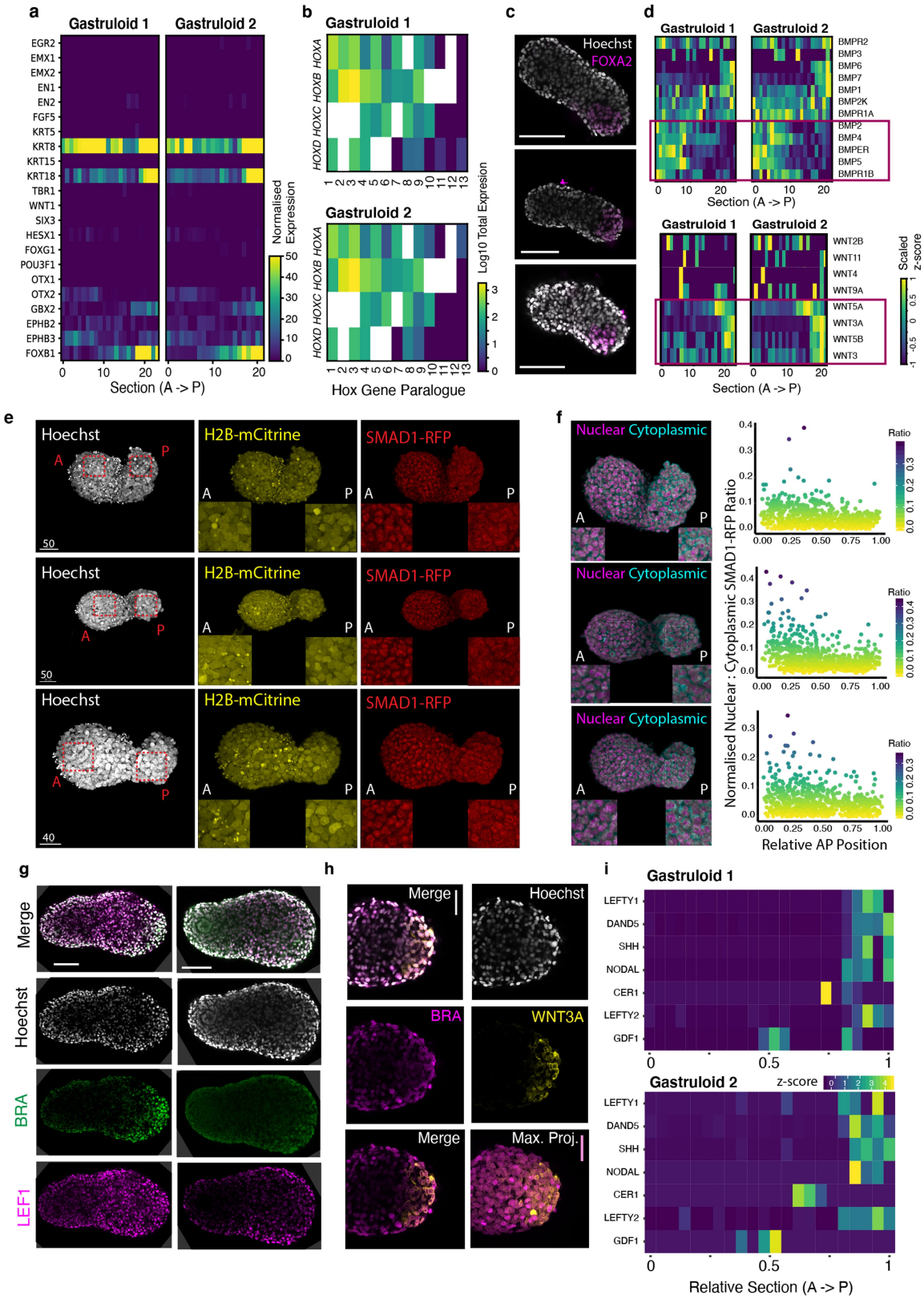

Extended Data Fig. 6 | See next page for caption.

Extended Data Fig. 6 | Transcriptional profiles and anteroposterior localization in human gastruloids. a, Normalized expression of anterior neural genes in human gastruloids. **b**, Total expression (log_{10}-transformed) of each HOX gene across all sections of gastruloid 1 (top) and gastruloid 2 (bottom), for all four clusters (HOXA, HOXB, HOXC and HOXD). White boxes indicate that a gene is not present in the human genome. $n = 2$ gastruloids (**a**, **b**). **c**, Expression of FOXA2 in the posterior end of 72-h Chiron-pre-treated RUES2-GLR gastruloids. Three representative examples are shown ($n = 8$ gastruloids). Scale bars, 100 µm. **d**, Expression of ligands of the BMP (top) and WNT (bottom) signalling pathways. Red box indicates genes with a particularly strong anteroposterior localization bias ($n = 2$ gastruloids). **e**, Maximum projection confocal images of SMAD1-RFP;H2B-mCitrine human gastruloids at 72 h. Three representative examples are shown. Insets, magnified views of the regions shown in red dashed boxes. Representative examples are shown ($n = 19$ gastruloids; two independent experiments). Scale bars; 40 µm or 50 µm (indicated on image). **f**, Processing to separate the nuclear and cytoplasmic component of the SMAD1–RFP signal (left; see Methods for details), and resultant quantification of the normalized nuclear:cytoplasmic ratio of SMAD1–RFP along the anteroposterior axis (right; each point represents a cell). Three representative examples are shown; two independent experiments. The scale of the images is the same as **e**. **g**, Immunostaining of LEF1 and BRA expression in 96-h RUES2-GLR human gastruloids. LEF1 is localized in a gradient primarily in the posterior portion of the gastruloids. Two representative examples are shown from three independent experiments ($n = 10$ gastruloids). Scale bars, 100 µm. **h**, Immunostaining of WNT3A and BRA expression in 72-h RUES2-GLR human gastruloids, showing a magnified view of the posterior end. Max. proj., maximum projection. One representative example is shown ($n = 8$ gastruloids; two independent experiments). Scale bars, 50 µm. **i**, Localized expression of genes that are related to Nodal signalling towards the posterior of Chiron-pre-treated human gastruloids by tomo-seq ($n = 2$ gastruloids).

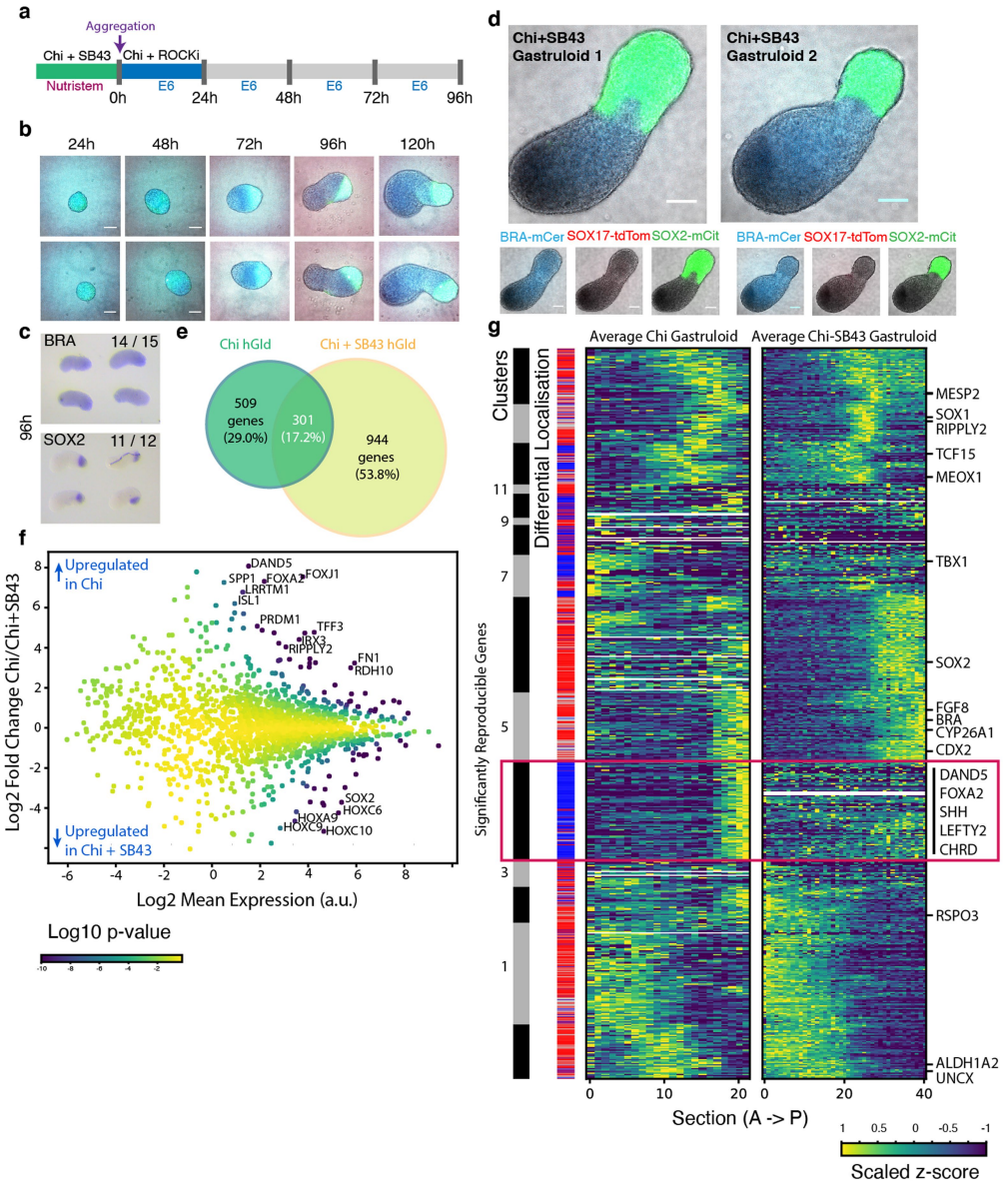

Extended Data Fig. 7 | Perturbation of Nodal signalling in human gastruloids. a, Schematic representation of the protocol used to generate Chiron and SB43 (Chi + SB43)-pre-treated human gastruloids. See Methods for details. **b**, Representative examples of the dynamic development of Chi + SB43-pre-treated RUES2-GLR gastruloids (three experiments). Colours indicate reporter fluorescence as indicated in Fig. 2a. Scale bars, 100 µm. **c**, In situ hybridization against *BRA* and *SOX2* mRNA in 96-h Chi + SB43-pre-treated gastruloids. Four representative examples are shown for each gene. **d**, Wide-field imaging of the two 120-h Chi + SB43-pre-treated RUES2-GLR gastruloids used for tomo-seq. Scale bars, 100 µm. **e**, Venn diagram showing the number of reproducibly localized genes in the Chiron-pre-treated (Chi hGld, green) and Chi + SB43-pre-treated (Chi + SB43 hGld, yellow) human gastruloids. Numbers indicate counts of genes and percentage values in brackets indicate the proportion of the full figure. See Source Data. **f**, Differentially expressed genes between Chiron-pre-treated and Chi + SB43-pre-treated gastruloids (total expression). See Methods, Supplementary Data 6, Source Data. **g**, Gene expression patterns detected in an averaged Chiron-pre-treated gastruloid and an averaged Chi + SB43-pre-treated gastruloid. Grey and black bands show the hierarchical clustering of gene expression; blue and red bands indicate selective reproducibility between replicates from one or other pre-treatment conditions (red, Chi + SB43 only; blue, Chiron only; grey; both); dark red box, cluster for which expression is lost after SB43 pre-treatment (cluster 4); white rows, no expression detected. $n = 2$ Chiron-pre-treated and $n = 2$ Chi + SB43-pre-treated gastruloids (**a**–**g**). See Methods, Supplementary Data 5, Source Data.

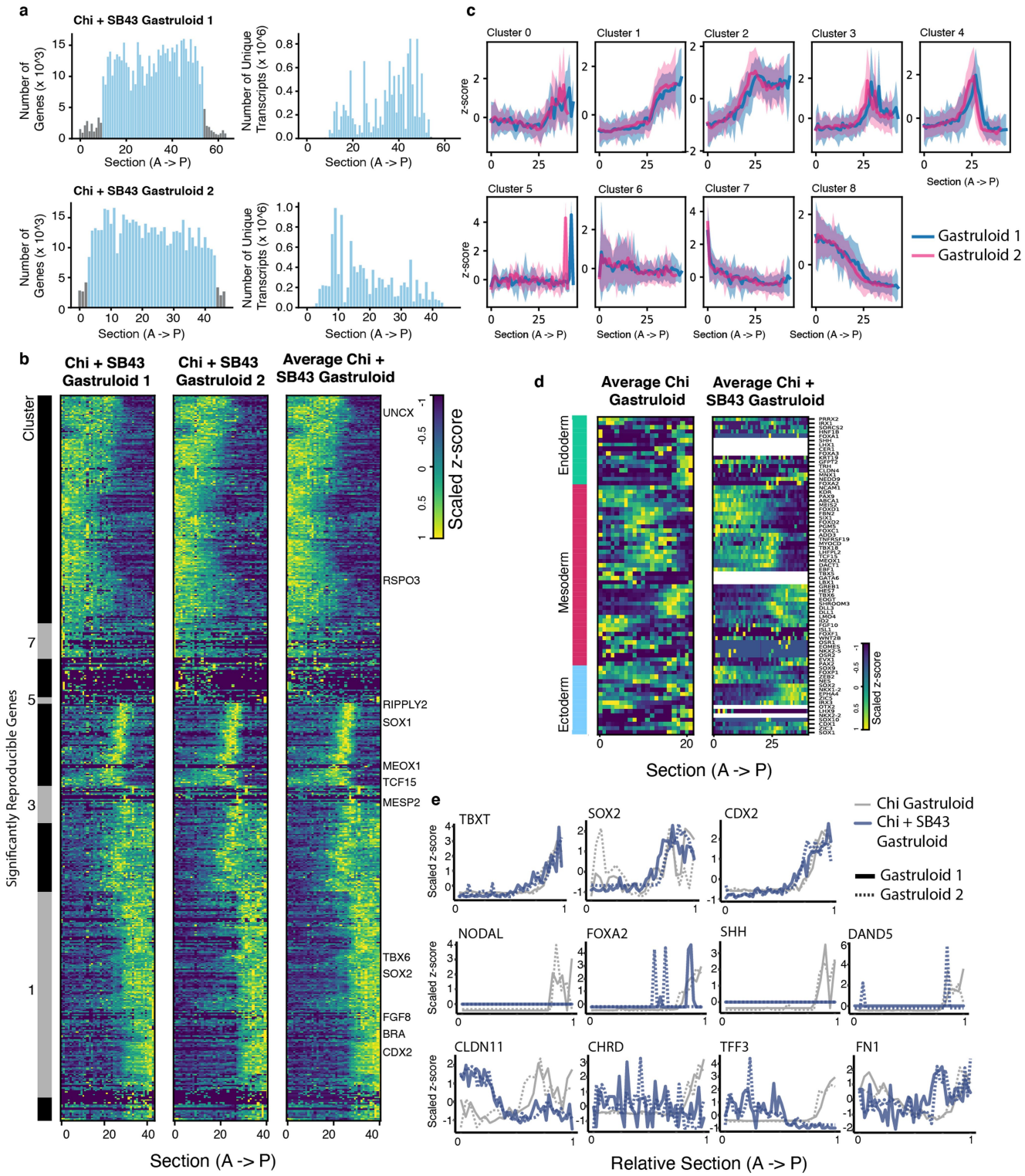

Extended Data Fig. 8 | Transcriptional profiles of gastruloids exposed to Nodal inhibition before aggregation. a, Quantification of the number of genes (left) and number of unique transcripts (right) detectable in each section along the anteroposterior axis of 120-h Chi + SB43-pre-treated RUES2-GLR gastruloids. Blue bars, sections above the threshold used for downstream tomo-seq analysis; grey bars, sections below the threshold (see Methods for details). Two replicates are shown. **b**, Significantly reproducible gene expression patterns of individual replicates of Chi + SB43-pre-treated human gastruloids (left) and the average gastruloid (right) along the anteroposterior axis. See Supplementary Data 4, Source Data. **c**, Average expression pattern of genes from each cluster shown in **b**. Lines, mean; shading, s.d. for the set of genes within each cluster. **d**, Detection of expression for markers of all three germ layers. White rows indicate that no expression was detected for that gene. See Supplementary Data 7, Source Data. **e**, Gene expression traces along the anteroposterior axis of the four human gastruloids (grey lines, Chiron pre-treatment; blue lines, Chi + SB43 pre-treatment; solid lines, replicate 1; dashed lines, replicate 2). $n = 2$ gastruloids (**a**–**e**).

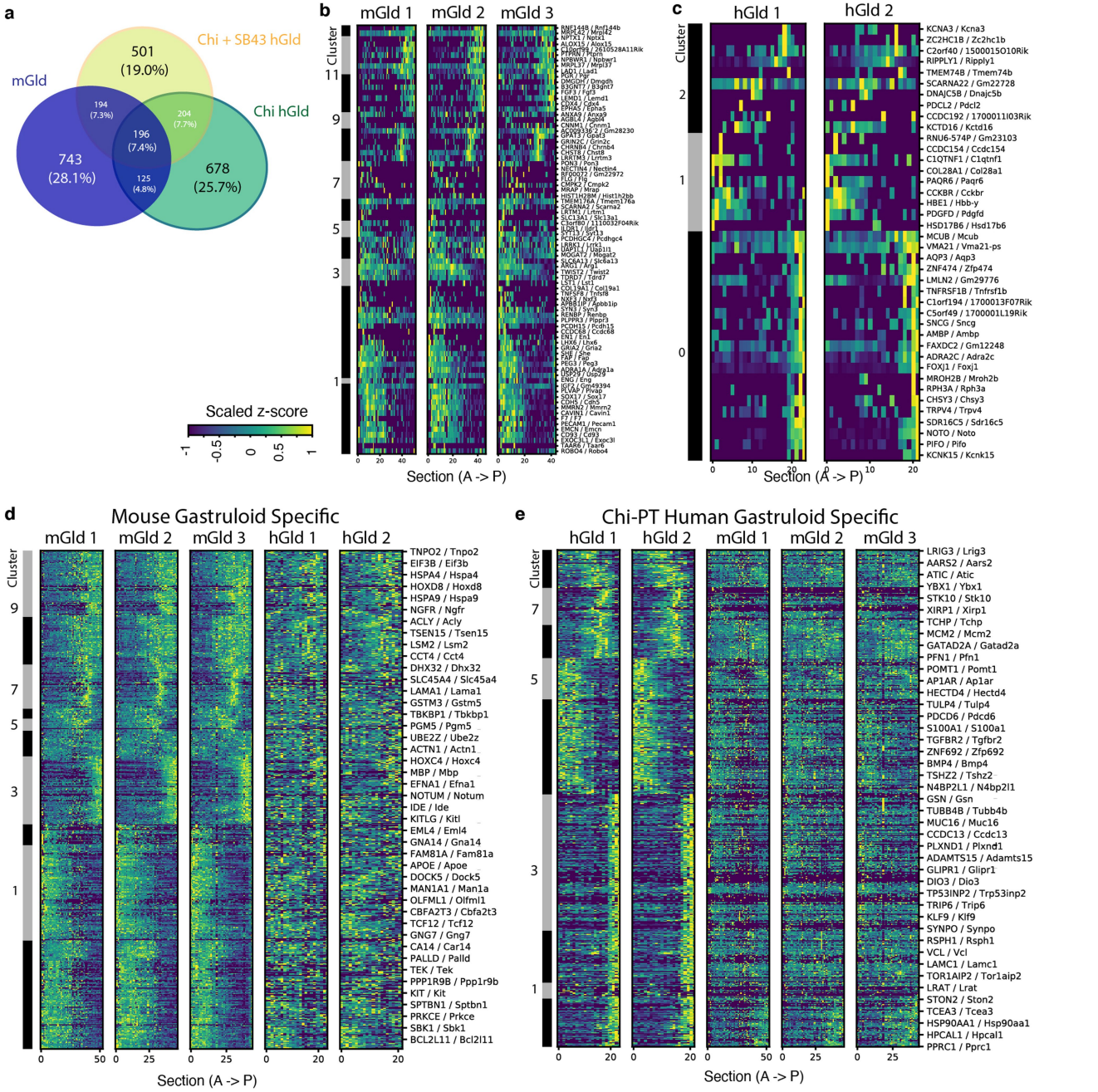

Extended Data Fig. 9 | Unique transcriptional profiles of mouse and human gastruloids. a, Venn diagram showing the number of common reproducibly localized genes in Chiron-pre-treated human gastruloids (Chi hGld, green), Chi + SB43-pre-treated human gastruloids (Chi + SB43 hGld, yellow) and mouse gastruloids (mGld, blue). Numbers indicate counts of genes and percentage values in brackets indicate the proportion of the full figure. **b**, Unique reproducibly localized gene expression in mouse gastruloids, not detected in Chiron-pre-treated human gastruloids. **c**, Unique reproducibly localized gene expression in Chiron-pre-treated human gastruloids, not detected in mouse gastruloids. **d**, Genes with reproducibly localized expression in mouse gastruloids and that are expressed, but not reproducibly localized, in Chiron-pre-treated human gastruloids. **e**, Genes with reproducibly localized expression in Chiron-pre-treated human gastruloids and that are expressed, but not reproducibly localized, in mouse gastruloids. $n = 2$ human gastruloids, $n = 3$ mouse gastruloids (**a**–**e**). See Supplementary Data 9, Source Data.

nature research

Corresponding author(s): Naomi Moris, Alfonso Martinez Arias, Alexander van Oudenaarden

Last updated by author(s): 21/01/2020

Reporting Summary

Nature Research wishes to improve the reproducibility of the work that we publish. This form provides structure for consistency and transparency in reporting. For further information on Nature Research policies, see Authors & Referees and the Editorial Policy Checklist.

Statistics

For all statistical analyses, confirm that the following items are present in the figure legend, table legend, main text, or Methods section.

n/a	Confirmed
☐	☒ The exact sample size (*n*) for each experimental group/condition, given as a discrete number and unit of measurement
☐	☒ A statement on whether measurements were taken from distinct samples or whether the same sample was measured repeatedly
☐	☒ The statistical test(s) used AND whether they are one- or two-sided *Only common tests should be described solely by name; describe more complex techniques in the Methods section.*
☒	☐ A description of all covariates tested
☒	☐ A description of any assumptions or corrections, such as tests of normality and adjustment for multiple comparisons
☐	☒ A full description of the statistical parameters including central tendency (e.g. means) or other basic estimates (e.g. regression coefficient) AND variation (e.g. standard deviation) or associated estimates of uncertainty (e.g. confidence intervals)
☐	☒ For null hypothesis testing, the test statistic (e.g. *F*, *t*, *r*) with confidence intervals, effect sizes, degrees of freedom and *P* value noted *Give P values as exact values whenever suitable.*
☒	☐ For Bayesian analysis, information on the choice of priors and Markov chain Monte Carlo settings
☒	☐ For hierarchical and complex designs, identification of the appropriate level for tests and full reporting of outcomes
☒	☐ Estimates of effect sizes (e.g. Cohen's *d*, Pearson's *r*), indicating how they were calculated

Our web collection on statistics for biologists contains articles on many of the points above.

Software and code

Policy information about availability of computer code

Data collection	Widefield image acquisition was performed with Zeiss AxioObserver.Z1 (Carl Zeiss, UK); Confocal image acquisition was performed with Zeiss Zen2010 v6. Code is available upon request to the authors.
Data analysis	RStudio Version 1.0.143, implementing the R software version 3.2.5 (2016-04-14) or 3.3.3 (2017-03-06), was used for statistical analysis; ImageJ/Fiji and Imaris were used for imaging data processing; Matlab and Python 3.6 were used for gastruloid image quantification and analysis. Code is available at https://github.com/vikas-trivedi/HumanGastruloids_Fluorescence, https://github.com/anna-alemany/humanGastruloids_tomoseq and https://github.com/naomi-moris/humanGastruloids_shapeDescriptors.

For manuscripts utilizing custom algorithms or software that are central to the research but not yet described in published literature, software must be made available to editors/reviewers. We strongly encourage code deposition in a community repository (e.g. GitHub). See the Nature Research guidelines for submitting code & software for further information.

Data

Policy information about availability of data

All manuscripts must include a data availability statement. This statement should provide the following information, where applicable:

- Accession codes, unique identifiers, or web links for publicly available datasets
- A list of figures that have associated raw data
- A description of any restrictions on data availability

All RNA-seq datasets produced in this study are deposited in the Gene Expression Omnibus (GEO) under accession code GSE123187. Source data for Figures 1-4 and Extended Data Figures 1-9 are provided within the manuscript files.

Field-specific reporting

Please select the one below that is the best fit for your research. If you are not sure, read the appropriate sections before making your selection.

☒ Life sciences ☐ Behavioural & social sciences ☐ Ecological, evolutionary & environmental sciences

For a reference copy of the document with all sections, see nature.com/documents/nr-reporting-summary-flat.pdf

Life sciences study design

All studies must disclose on these points even when the disclosure is negative.

Sample size	Sample sizes were not predetermined. For gene expression pattern analysis by widefield or immunofluorescence imaging, multiple gastruloids were used to test the reproducibility of the results across biological replicates. For spatial transcriptomic studies we used two human gastruloid replicates for each condition. This number was enough to identify significantly reproducible genes, with little variance between replicates.
Data exclusions	No data were excluded from the analysis, except in automated image analysis where empty wells or debris were present; this criteria was pre-established.
Replication	Replication of experimental procedures was performed, as noted in the text, to verify the reproducibility of the results. Each individual experiment contained technical replicates. All attempts at replication were successful.
Randomization	Randomization was not relevant to our study, as experimental group allocation was not used.
Blinding	Our study did not use any blinding for data collection or analysis.

Reporting for specific materials, systems and methods

We require information from authors about some types of materials, experimental systems and methods used in many studies. Here, indicate whether each material, system or method listed is relevant to your study. If you are not sure if a list item applies to your research, read the appropriate section before selecting a response.

Materials & experimental systems

n/a	Involved in the study
☐	☒ Antibodies
☐	☒ Eukaryotic cell lines
☒	☐ Palaeontology
☒	☐ Animals and other organisms
☒	☐ Human research participants
☒	☐ Clinical data

Methods

n/a	Involved in the study
☒	☐ ChIP-seq
☒	☐ Flow cytometry
☒	☐ MRI-based neuroimaging

Antibodies

Antibodies used	1:200 Rabbit anti-CDX2 (ThermoScientific, EPR2764Y, LOT:211651805F); 1:200 Goat anti-GATA6 (R&D Systems, AF1700, LOT:KWT0112101); 1:200 Rabbit anti-BRACHYURY (AbCam, ab209665, LOT:GR3268140-1); 1:200 Goat anti-BRACHYURY (Santa Cruz, sc17743, LOT:E1616), 1:200 Goat anti-SOX2 (R&D Systems, AF2018, LOT:KOY0213101); 1:200 Mouse anti-CDH2 (BD Biosciences, BD10920); 1:200 Rat anti-CDH1 (Takara, M108), 1:100 Rabbit anti-Wnt3a (AbCam, ab219412, LOT:GR3220844-2), 1:200 Rabbit anti-LEF1 (AbCam, ab137872, LOT:GR3236752-4), 1:200 Rabbit anti-FOXA2 (AbCam, ab108422, LOT:GR3250052-5), 1:200 mouse anti-NOTCH1 (BD Biosciences, 552466, LOT:4345524), 1:200 anti-RFP (AbCam, ab62341, LOT:GR257333-6). All secondary antibodies were all diluted 1:500, and included Alexa-Fluor-488, -568 and -647 conjugated antibodies (Invitrogen).
Validation	All primary antibodies have been validated for use with immunofluorescence in human cells by the manufacturers, and were tested for specific signal (and low background) in our system.

Eukaryotic cell lines

Policy information about cell lines

Cell line source(s)	The cell lines used in this study include the hESC lines: MasterShef7 (Canham, M. A. et al. The Molecular Karyotype of 25 Clinical-Grade Human Embryonic Stem Cell Lines. Sci Rep 5, 17258, doi:10.1038/srep17258 (2015).), S4-GATA6-GFP (Allison, T. F. et al. Identification and Single-Cell Functional Characterization of an Endodermally Biased Pluripotent Substate in Human Embryonic Stem Cells. Stem cell reports 10, 1895-1907, doi:10.1016/j.stemcr.2018.04.015 (2018).), RUES2-GLR (Martyn, I., Kanno, T. Y., Ruzo, A., Siggia, E. D. & Brivanlou, A. H. Self-organization of a human organizer by combined Wnt and Nodal

	signalling. Nature 558, 132-135, doi:10.1038/s41586-018-0150-y (2018).) and RUES2:SMAD1-RFP;H2B-mCitrine (Yoney, A. et al. WNT signaling memory is required for ACTIVIN to function as a morphogen in human gastruloids. Elife 7, doi:10.7554/eLife.38279 (2018).). All were provided as gifts from the respective lab groups.
Authentication	All lines were able to maintain sustained pluripotency under standard hESC pluripotent culture conditions, and differentiate in culture. Fluorescent reporter signal was assessed by widefield microscopy.
Mycoplasma contamination	The cell lines were not tested for mycoplasma contamination.
Commonly misidentified lines (See ICLAC register)	No commonly misidentified cell lines were used in this study.